

GNSS interference mitigation: A measurement and position domain assessment

Daniele Borio  | **Ciro Gioia** 

European Commission, Joint Research
Centre (JRC), Italy

Correspondence

Daniele Borio, Ispra (VA), Italy.
Email: daniele.borio@ec.europa.eu

Abstract

Modern Global Navigation Satellite System (GNSS) receivers have to withstand significant levels of interference in order to operate under harsh conditions, such as in the presence of jamming and of other Radio Frequency (RF) threats. A possibility is to implement pre-correlation interference mitigation techniques that operate directly on the samples provided by the receiver front-end. This paper provides an assessment of five interference mitigation techniques at the measurement and position level. The analysis focuses on the Adaptive Notch Filter (ANF) and on four Robust Interference Mitigation (RIM) techniques. Several data collections were performed in the presence of jamming, and the data collected were used for the analysis that shows that RIM techniques do not introduce biases at both the measurement and position level. While the ANF delays pseudorange measurements, the biases introduced are predominantly common to all the observations with a negligible impact on a Single Point Positioning (SPP) solution.

KEYWORDS

Adaptive Notch Filter, GNSS, Interference, Jamming, Robust Interference Mitigation

1 | INTRODUCTION

Over the last decade, the RF environments where GNSS receivers are required to operate have significantly evolved with the proliferation of interference sources and of other threats to GNSS operations (Ioannides et al., 2016; Pattinson et al., 2017). The EU-funded Standardisation of GNSS Threat reporting and Receiver testing through the International Knowledge Exchange, Experimentation and Exploitation (STRIKE3) project deployed monitoring stations in several locations around the world (Pattinson et al., 2017): over two years of operations, more than 300,000 interference events were recorded by the STRIKE3 monitoring system and around 10% of such events were jamming attacks (Pattinson et al., 2017). Jamming is a form

of Denial of Service (DoS) attack usually performed using low cost devices, called jammers, that transmit significant power in the GNSS bands preventing signal reception (Borio et al., 2016; Gao et al., 2016). In order to cope with interference and jamming, receiver manufacturers are improving receiver design and adopting detection and mitigation techniques, which can enable GNSS signal reception even in the presence of significant levels of interference (De Wilde et al., 2015; Di Grazia et al., 2019; Willems & De Wilde, 2013). There exist several algorithms for interference mitigation, and the most popular ones are probably Pulse Blanking (PB) (Gao et al., 2013, 2016) for reducing the impact of pulsed interference and notch filtering (Borio et al., 2006; Calmettes et al., 2001) for Continuous Wave (CW) removal. These techniques are

This is an open access article under the terms of the [Creative Commons Attribution](https://creativecommons.org/licenses/by/4.0/) License, which permits use, distribution and reproduction in any medium, provided the original work is properly cited.

© 2020 European Union. NAVIGATION published by Wiley Periodicals LLC on behalf of Institute of Navigation.

pre-correlation in the sense that they operate directly on the samples provided by the receiver front-end before the correlation process. These techniques are signal processing approaches that can significantly improve receiver performance and allow positioning in severe RF conditions. On the other hand, the use of filters and other interference mitigation techniques can introduce biases in the GNSS measurements. For example, a notch filter with fixed notch frequency can introduce biases that can be estimated and compensated (Di Grazia et al., 2019; Raasakka & Orejas, 2014; Qin, Troglia Gamba et al., 2019; Giordanengo, 2009).

In addition to notch filtering and PB, the framework of RIM has been recently introduced (Borio, 2017a, 2017b) to mitigate the impact of interference by exploiting principles from robust statistics (Huber, 1964; Huber & Ronchetti, 2009). Several RIM techniques have been proposed, and PB can be considered as a special form of RIM. Each technique has specific characteristics and different computational requirements.

While significant work has been devoted to characterize RIM techniques at the signal processing level, limited analysis has been performed in order to assess the impact of these approaches in the measurement and position domains. This paper studies the impact of RIM at the measurement and position level, investigating the potential introduction of biases and of additional measurement noise. In addition to RIM, the ANF (Borio et al., 2006; Calmettes et al., 2001) is also considered as a comparison term. In this way, a total of five interference mitigation techniques are analyzed as discussed in Section 2.

The analysis has been conducted by using real GNSS data collected in the presence of jamming components transmitted by real jammers. For this purpose, a Universal Software Radio Peripheral (USRP) 2 was used to collect In-phase Quadrature (I/Q) data that were then processed using a custom Matlab software receiver. A dedicated experimental setup was developed where jammed GNSS signals were obtained. The experimental setup adopted is fully described in Section 5 and led to progressively increasing levels of jamming power. In this way, it was possible to study measurements and position solutions as a function of the Jamming to Noise power ratio (J/N).

Three GNSS signals were considered for the analysis: GPS L1 Coarse Acquisition (C/A) signals, the Binary Offset Carrier (BOC) modulation adopted by Galileo E1b/c signals, and the wideband Binary Phase Shift Keying (BPSK) modulation adopted by the Galileo E5b component. For both E1b and E5b signals, pilot processing was implemented.

The custom software receiver was used to generate Receiver Independent Exchange Format (RINEX) files that were used for the measurement and position domain analysis. The same datasets were processed using standard

processing and the different interference mitigation techniques. The analysis focuses on pseudoranges and on SPP where the final position solution is obtained using a Weighted Least Squares (WLS) approach (Misra & Enge, 2006). The analysis of carrier phase observations and carrier phase positioning techniques is out of the scope of this paper and is left for future work.

The experimental setup, which adopts real jamming signals, and the analysis of three different GNSS modulations provide a unified testing of the five interference mitigation techniques considered. We also provide a new perspective on the ANF that was mainly analyzed in the presence of Continuous Wave Interference (CWI) or at the signal processing level. For instance, Raasakka and Orejas (2014) evaluated the distortions introduced by the ANF when mitigating the impact of CWs with a fixed frequency. Giordanengo (2009) studied the distortions introduced by notch filters on the useful signal correlation function. However, only non-adaptive notch filters with a fixed notch were analyzed. Moreover, the impact on pseudoranges was not considered. Qin, Troglia Gamba, et al. (2019); Qin, Dovis, et al. (2019); and Borio et al. (2012) studied the ANF at the signal processing level without considering measurement generation and position solution. While introduced as a comparison term, the results obtained in this paper show additional properties of the ANF that is evaluated in the presence of real jamming signals. These signals make the center frequency of ANF vary in a fast way, modifying the type of distortions observed for the processing of CWI.

From the analysis, it emerges that RIM techniques do not introduce biases at both the measurement and position level. In contrast, the ANF introduces biases on the pseudoranges. These biases are difficult to predict, most of all when the parameters of the filters are varying rapidly for tracking the jamming component. In this respect, different delays were observed for different jamming power conditions. These biases are mostly common-mode to all the observations, and no effects were found in the final SPP solution when using the ANF. Additional analysis is required to assess the impact of the ANF on carrier phase-based position solutions.

The paper also discusses the impact of interference mitigation on the variance of the measurements and of the final position solution. Two working conditions are analyzed: 1) in the absence of interference and 2) for significant levels of jamming. In the absence of interference, the expected degradation is quite limited and determined by the Loss of Efficiency (LoE) caused by interference mitigation on the processing of the individual GNSS signal. In practice, this loss is not observed because of the imperfections caused by the receiver front-end. For example, the USRP 2 front-end has a poor clock and introduces a CW (Peng & Morton, 2013), which is mitigated by the approaches analyzed.

In this way, the LoE is partially compensated for, and no significant noise increase is found in the final position solution. In real receivers, such as those integrated inside smartphones, spurious and CWs generated by nearby electronic components are commonly present. Since we were aiming at realistic testing conditions, such effects were not mitigated using, for example, an external clock reference.

In the presence of significant levels of jamming, the performance of the different mitigation techniques depends on the type of signal to be mitigated and on the parameters selected. For example, for pulsed interference, time-domain techniques such as PB and the complex signum non-linearity (Borio & Closas, 2018) provide significant improvements whereas frequency domain techniques can worsen the receiver performance. In our experimentation, one RIM technique, Frequency Domain Pulse Blanking (FDPB), is outperformed by standard processing. This is due to the nature of the jamming signal and to an improper selection of the FDPB decision threshold. This result highlights the fact that mitigation techniques are effective only for specific classes of interference. A discussion on the different approaches for selecting the parameters of interference mitigation techniques is provided in Section 2.3.

This paper is an extended version of a conference paper (Borio & Gioia, 2020). With respect to Borio and Gioia (2020), this paper provides additional theoretical results and introduces the ANF that is used as a comparison term.

The remainder of this paper is organized as follows: interference mitigation techniques are briefly described in Section 2 whereas the approach adopted for measurement domain and position domain analysis is detailed in Section 3. Theoretical results for the LoE are provided in Section 4. The experimental setup and the different tests conducted are described in Section 5, and experimental results are provided in Section 6. Conclusions are finally drawn in Section 7.

2 | GNSS INTERFERENCE MITIGATION

In this section, the techniques considered for the mitigation of jamming signals are briefly described: the ANF is introduced in Section 2.1, while RIM techniques are presented in Section 2.2. It is assumed that GNSS signals have been collected and digitized by the receiver front-end, which provides a discrete base-band representation of the signals at the receiver antenna. In this way, the signal

$$y[n] = s[n] + \eta[n] + i[n] \quad (1)$$

is obtained. The three terms in Equation (1) are the useful GNSS signal components, $s[n]$, a noise term modeled as Additive White Gaussian Noise (AWGN), $\eta[n]$, and an

interference term, $i[n]$. $y[n]$ has been sampled at the frequency, f_s , and n is used to denote the time index. All the five techniques considered here directly act on $y[n]$. Additional details on the signals at the output of the receiver front-end can be found in Tsui (2004) and Kaplan and Hegarty (2005).

Interference mitigation techniques output a new set of samples, $\tilde{y}[n]$, that are then provided to the standard signal processing blocks, acquisition, and tracking. These blocks provide the final measurements: pseudoranges, Doppler shifts, carrier phases, and Carrier-to-Noise power spectral density ratio (C/N_0) estimates. These measurements are then used for the computation of the user position. In the following, the focus will be on pseudoranges and on a SPP solution.

2.1 | Adaptive notch filter

The ANF is an enhanced version of the traditional notch filter (Borio et al., 2008) where the frequency of the notch is adapted in order to track the variations of the jamming signal. The filter removes jamming signals by placing a frequency notch in correspondence of the estimated jamming frequency. The ANF is a linear operator, and its transfer function is given by Borio et al. (2006):

$$H_{ANF}(z) = \frac{1 - z_0 z^{-1}}{1 - k_\alpha z_0 z^{-1}}, \quad (2)$$

where z_0 is the zero of the filter and k_α is the pole contraction factor, which assumes values between zero and one. The output of the ANF is defined by Equation (2), and it is given by

$$\tilde{y}[n] = y[n] - z_0 y[n-1] + k_\alpha z_0 \tilde{y}[n-1]. \quad (3)$$

The zero of the ANF, z_0 , should be selected in order to have

$$\tilde{i}[n] = i[n] - z_0 i[n-1] \approx 0 \quad (4)$$

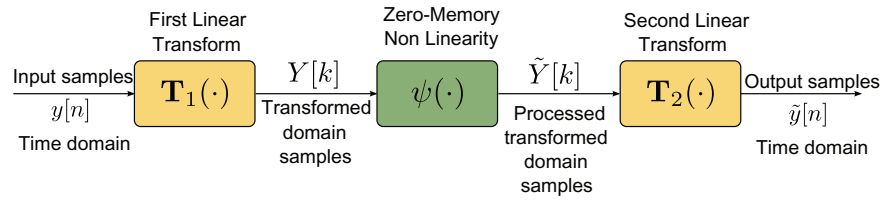
and to preserve the useful signal components. Condition (4) establishes a recurrence equation that defines the class of interfering signals that can be effectively mitigated by the ANF.

The frequency of the notch can be expressed as

$$f_0 = \frac{f_s}{2\pi} \angle z_0. \quad (5)$$

The notch placed around f_0 by transfer function (2) allows the removal of the signal components located around the notch frequency. The ANF has an adaptation block, which continuously tracks the center frequency of the input jamming signal: when f_0 is close to the instantaneous frequency of the jamming signal, then the interference

FIGURE 1 Schematic representation of RIM techniques. [Color figure can be viewed in the online issue, which is available at wileyonlinelibrary.com and www.ion.org]



term is removed. The adaptation block of the ANF operates by minimizing the energy of the samples at its output. It implements a gradient descent algorithm whose speed is governed by the adaptation step, δ .

2.2 | Robust interference mitigation

RIM techniques are characterized by the common structure shown in Figure 1 (Borio & Gioia, 2020). The input samples are at first brought in a transformed domain where the interference term, $i[n]$, admits a sparse representation. In particular, the transformed domain samples, $Y[k]$, are obtained as

$$Y[k] = T_1(y[n]). \quad (6)$$

$T_1(\cdot)$ defines a linear transform where a vector of N samples is transformed in a new vector whose samples are denoted by $Y[k]$. This transform can be represented as a matrix multiplication. The goal of this transform is to bring the interference term, $i[n]$, in a domain where it admits a sparse representation. In this domain, only a few samples are affected by interference. While several transform domains exist (Musumeci & Dovic, 2015a), two transforms are considered in the following:

- the **identity** transform, which corresponds to using the original samples, $y[n]$. In this case, RIM techniques operates in time domain,
- the **Discrete Fourier Transform (DFT)**, which corresponds to project the input samples in the frequency domain.

A Zero Memory Non-Linearity (ZMNL) is then applied to the transformed domain samples, $Y[k]$. This non-linearity preserves the phase information of the samples but de-weights their amplitude if identified as outliers (Borio & Closas, 2019). Common non-linearities are

- **pulse blanking**:

$$\tilde{Y}[k] = \psi(Y[k]) = \begin{cases} Y[k] & \text{if } |Y[k]| < T_h \\ 0 & \text{otherwise} \end{cases}, \quad (7)$$

where T_h is a decision threshold to be fixed by the user, and

- **the complex signum** (Borio & Closas, 2018):

$$\tilde{Y}[k] = \text{csign}(Y[k]) = \frac{Y[k]}{|Y[k]|}. \quad (8)$$

After applying the ZMNL, the transformed domain processed samples, $\tilde{Y}[k]$, are obtained. Finally, these samples are brought back in the time domain using a second linear transform, $T_2(\cdot)$:

$$\tilde{y}[n] = T_2(\tilde{Y}[k]). \quad (9)$$

When time domain is implemented, $T_2(\cdot)$ also corresponds to the identity transform. Note that for time domain processing, linear filters can also be used to protect the main frequency components of GNSS signals. In this work, only the case where identity transforms are used is considered. If frequency domain processing is adopted, $T_2(\cdot)$ is the Inverse DFT (IDFT).

Combining the two ZMNLs and the two processing domains, the following four RIM techniques are obtained:

- Time Domain Complex Signum (TDCS),
- Time Domain Pulse Blanking (TDPB),
- Frequency Domain Complex Signum (FDCS),
- FDPB.

TDPB corresponds to standard PB whereas FDPB is a form of frequency excision (Musumeci & Dovic, 2015b; Young & Lehnert, 1998).

2.3 | Parameter selection

The performance and behavior of parametric interference mitigation techniques, such as the ANF and PB, are strongly influenced by their parameter values. These parameters should be set according to the characteristics of the jamming signals and failing their selection may lead to significant performance degradation as demonstrated in the following for the FDPB technique.

In this section, a summary of the approaches used in the literature for setting the ANF and PB parameters is provided along with typical values. The two techniques based on the complex signum non-linearity are parameter-free:

this is one of the main advantages of this class of algorithms (Borio & Closas, 2018).

The ANF is characterized by two parameters: the pole contraction factor, k_α , and the adaptation step, δ . The pole contraction factor, k_α , depends on the type of signals at the input of the ANF. In particular, values closed to unity are suitable for CWI whose frequency is stable over time. Smaller k_α values are required to track swept jamming signals (Borio et al., 2012; Qin, Dovis, et al., 2019; Qin, Troglia Gamba, et al., 2019; Troglia Gamba et al., 2012; Wendel et al., 2016).

Theoretical foundations for the ANF were provided in Calmettes et al. (2001) that considered k_α values in the [0.95, 0.99] ranges. These values were derived from theoretical considerations on the filter steady-state error and were not confirmed by experimentation. Moreover, the proposed values did not consider the effect of fast varying jamming signals with potentially discontinuous instantaneous frequencies. A real implementation on a Field-Programmable Gate Array (FPGA) platform was considered in Troglia Gamba et al. (2012) for CWI removal: it was shown that a $k_\alpha = 0.99$ was placing the filter pole too close to the unit circle creating stability and convergence problems. It was suggested to use k_α in the [0.9, 0.98] range. Also, Raasakka and Orejas (2014) analyzed the ANF in the presence of CWI using a Spirent simulator and a Honeywell receiver prototype. In this case, a pole contraction factor equal to 0.9 was selected in agreement with the results obtained by Troglia Gamba et al. (2012).

The problem of selecting k_α in the presence of swept interference was addressed in Qin, Dovis, et al. (2019) and Qin, Troglia Gamba, et al. (2019) that optimized k_α with respect to the Peak-to-Noise floor Ratio (PNR) in acquisition, the tracking error and the residual Interference Error Envelope (IEE). It was shown that, for this type of signals, best performance is achieved for $k_\alpha \in [0.7, 0.9]$. These results are confirmed by the experiments conducted in Wendel et al. (2016) and Borio et al. (2012). Wendel et al. (2016) also analyzed the limits of the ANF that cannot track excessively fast varying jamming signals. These results support the fact that a k_α should be selected in the [0.7, 0.9] for tracking swept interfering signals. For this reason, we considered $k_\alpha = 0.8$ and $k_\alpha = 0.9$ as a compromise between notch width and adaptation speed.

The selection of the adaptation step, δ , depends on k_α and, in particular, Calmettes et al. (2001) showed that

$$\delta < \sqrt{\frac{1 - k_\alpha}{4}}, \quad (10)$$

which implies that δ should be reduced as k_α gets close to one. In this way, the ability of the ANF to track fast-

varying interference frequencies is further reduced. Qin, Dovis, et al. (2019) and Qin, Troglia Gamba, et al. (2019) also analyzed the impact of δ on the acquisition PNR, on the tracking error, and on the IEE. Effective values of δ are in the [0.001, 0.1] range. Large values of δ can, however, lead to instability problems. For this reason, Wendel et al. (2016) used $\delta = 0.025$, which is the same value adopted in this paper.

In PB, the selection of the blanking threshold often requires a calibration step (Bastide et al., 2004; Hegarty et al., 2000; Raimondi et al., 2008) where the noise floor at the receiver input is estimated in the absence of interference. This step is required since T_h is, in general, selected as a function of the noise floor (Musumeci & Dovis, 2015b):

$$T_h = \alpha_T \sigma = \alpha_T \sqrt{\text{Var}\{\eta[n]\}}, \quad (11)$$

where σ is the standard deviation of the input noise, $\eta[n]$. If a frequency domain approach is used, σ is the standard deviation of the Transformed Domain (TD) samples in the absence of interference. Thus, PB requires the estimation of σ that can be determined *a priori*, during the calibration stage, or using power/amplitude estimation algorithms (Rugamer et al., 2017). α_T is a constant usually selected after an optimization process (Bastide et al., 2004; Raimondi et al., 2008), by fixing a predefined level of false alarm probability (Wang et al., 2010) or according to heuristic approaches. In the absence of interference, the input samples should approximately follow a Gaussian distribution. Thus, α_T should be selected such that only a limited number of samples passes the blanking threshold without being affected by interference. For example, when a real sampling scheme is used (Tsui, 2004), the probability that a sample passes $T_h = 3\sigma$ is equal to $2.7 \cdot 10^{-3}$. If a complex I/Q sampling scheme is used, the probability that the amplitude of a clean sample passes the threshold becomes $1.23 \cdot 10^{-4}$. For this reason, in the following, $\alpha_T = 3$ was selected. For the experiments, σ was estimated using a block of clean data collected in the absence of interference. σ was kept constant during the whole duration of the tests.

Other approaches for fixing T_h require specific loss models (Bastide et al., 2004; Raimondi et al., 2008). α_T is then selected by minimizing the expected loss. Loss models are, however, derived for specific signal classes such as Distance Measurement Equipment (DME) and TACTical Air Navigation system (TACAN) (Bastide et al., 2004; Raimondi et al., 2008) and can be hardly applied to other modulations.

Finally, in TDPB and in the presence of a limited number of bits for signal quantization, T_h can be set by taking into account the Automatic Gain Control (AGC) response and the number of quantization levels. The AGC estimates the noise power at the input of the Analog-to-Digital

TABLE 1 Interference mitigation parameters and typical values

Technique	Parameter	Value	Comments and references
ANF	Pole contraction factor, k_α	[0.7,0.9]	For swept interference (Borio, O'Driscoll, and Fortuny, 2012; Qin, Dosis, et al., 2019; Qin, Troglia Gamba, et al., 2019; Troglia Gamba et al., 2012; Wendel et al., 2016)
		[0.9,0.98]	For CWI (Calmettes et al., 2001; Raasakka & Orejas, 2014; Troglia Gamba et al., 2012)
	Adaptation step, δ	$\delta < \sqrt{\frac{1-k_\alpha}{4}}$, [0.001,0.1]	(Calmettes et al., 2001; Qin et al., 2019; Wendel et al., 2016)
PB	Decision Threshold, T_h	$\alpha_T \sigma$	Require noise floor estimation (Bastide, Chatre et al., 2004; Raimondi et al., 2008; Rugamer et al., 2017; Wang et al., 2010)
		quantization level	Noise floor estimated by the AGC (Bastide, Macabiau et al., 2003; Borio & Cano, 2013; Hegarty et al., 2000)
complex signum	Parameter free		(Borio & Closas, 2018)

Converter (ADC) and scales the input analog signal in order to fully exploit the ADC dynamic. When TDPB is used, the AGC should be able to estimate the noise power without being significantly affected by the interference pulses (Bastide et al., 2003; Hegarty et al., 2000). Then, the last bit of the ADC is used for pulse detection. For example, Bastide et al. (2003) considered a symmetric 4-bit ADC. The AGC was configured to obtain an optimal 3-bit loading: samples characterized by a fourth bit equal to one were detected as interference pulses. A general approach for fixing T_h in the presence of a limited number of bits was proposed in Borio and Cano (2013).

In the discussion provided above, no distinction was made between time and frequency domain approaches. The principles analyzed for setting the blanking threshold are general and valid independently from the processing domain. TD processing can be implemented in several ways including the usage of pre-weighting and with and without overlapping analysis windows (Gevargiz et al., 1984; Musumeci & Dosis, 2015b; Young & Lehnert, 1999). The analysis of these techniques and of their parameters is out of the scope of this paper. In the following, the simplest approach without weighting and window overlapping has been adopted.

A summary of the typical values adopted for the parameters of the different interference mitigation techniques is provided in Table 1.

3 | MEASUREMENT AND POSITION DOMAIN ANALYSIS

The approaches used for evaluating the impact of RIM in the measurement and position domains are presented in

this section. The evaluation exploits the methods proposed in Borio and Gioia (2020) and Rao et al. (2014) where measurements and position solutions obtained using different processing schemes are compared. In the measurement domain, the analysis focuses on pseudoranges; in order to assess the impact of the different interference mitigation strategies, a comparison with respect to standard processing was carried out. Specifically, for each interference mitigation strategy, the difference between pseudoranges computed with and without mitigation was formed:

$$PR_{diff}[t] = PR_{Mit}[t] - PR_{Standard}[t], \quad (12)$$

where $PR_{diff}[t]$ is the pseudorange difference at the epoch t and PR_{Mit} and $PR_{Standard}$ are the pseudoranges obtained with and without interference mitigation. This approach leads to the cancellation of all the common errors preserving the differences introduced by the specific processing scheme.

In order to analyze the impact of interference mitigation on the position solution, positioning errors were computed for all the processing strategies considered. The analysis focused on SPP computed using a WLS approach (Gioia & Borio, 2016; Hoffmann-Wellenhof et al., 1992). Weights were determined using the satellite elevation (Gioia, 2014; Kuusniemi, 2005). Since the antenna of the receiver was carefully surveyed, it was possible to compute position errors with respect to the known antenna location. The errors were computed in a local East, North, Up (ENU) frame centered into the antenna reference position. In this way, it was possible to directly compare the position errors and analyze the impact of interference mitigation.

It is noted that the first part of three tests described in Section 5 is characterized by low levels of jamming. In this

way, it was also possible to analyze the impact of interference mitigation in the absence of interference.

4 | LOSS OF EFFICIENCY

In this section, the impact of interference mitigation is discussed from a theoretical standpoint, and its effect is propagated from the correlator output to the measurements and to the final position solution. The analysis is performed in terms of measurement and position variances.

RIM techniques are obtained by modeling the noise affecting the input samples with probability density functions (pdfs) with tails heavier than those of the Gaussian distribution (Borio, 2017a; Borio & Closas, 2018). Standard acquisition and tracking algorithms are the solution of a Minimum Mean Square Error (MMSE) problem derived under the hypothesis that the input samples are affected by Gaussian noise only. In the presence of interference, this hypothesis is no longer true and robust approaches can be adopted. On the other hand, robust approaches are sub-optimal when only noise is present and the Gaussian hypothesis holds true (Medina et al., 2019). In particular, a loss is introduced at the correlator output and a lower coherent output Signal-to-Noise Ratio (SNR) is obtained with respect to standard approaches (Borio, 2017a; Borio & Closas, 2019). The coherent output SNR is the ratio between the peak of the signal Cross Ambiguity Function (CAF) and the noise floor, and it is defined as (Betz, 2000, 2001)

$$\text{SNR}_{out} = \max_{\tau, f_d} \frac{|E[C(\tau, f_d)]|^2}{\frac{1}{2} \text{Var}\{C(\tau, f_d)\}}, \quad (13)$$

where $C(\tau, f_d)$ is the signal CAF and τ and f_d are the code delay and Doppler frequency, respectively. When the receiver tracking loops are able to lock on the useful signal component, the code delay and Doppler frequency of the received signal are properly estimated, and the CAF is maximized. The maximization in Equation (13) implies that the coherent output SNR should be measured under lock conditions. In this respect, SNR_{out} can be interpreted as the square magnitude of the average of the Prompt correlation normalized by half its variance. The half term is due to the fact that also phase lock conditions should be achieved. When this happens, all the signal energy is in the in-phase component whereas the quadrature channel contains only noise. Thus, half of the noise power can be removed by considering only the in-phase component.

When RIM techniques are used and the Gaussian model holds true, a lower coherent output SNR is obtained

with respect to the ideal one obtained with standard processing:

$$\text{SNR}_{out}^{Mit} = L_o \text{SNR}_{out}, \quad (14)$$

where SNR_{out}^{Mit} is the SNR obtained when interference mitigation is applied and L_o is the LoE. Note that Equation (14) is also valid for the ANF (Borio et al., 2006).

Under ideal conditions, i.e., when only Gaussian noise is present and when the impact of front-end filtering is neglected, the coherent output SNR is related to the input C/N_0 by (Betz, 2000, 2001)

$$\text{SNR}_{out} = 2 \frac{C}{N_0} T_c, \quad (15)$$

where T_c is the coherent integration time used for the computation of the CAF and of the correlators. Relationship (15) can be used to propagate the impact of interference mitigation back to the input C/N_0 . This approach was developed by Betz (2000, 2001) that introduced the concept of effective C/N_0 . In particular, the effect of mitigation techniques in the absence of interference can be modeled by introducing an equivalent loss on the effective C/N_0 . The proportionality relationship defined in Equation (15) implies that the loss in terms of effective C/N_0 is equal to L_o .

When analyzing the impact of mitigation techniques on pseudorange measurements, standard formulas can be used (Misra and Enge, 2006, p. 482; Van Dierendonck, 1996, p. 374)

$$\sigma_\tau^2 \approx \frac{B_L d}{2C/N_0} T_{chip}^2 \quad [\text{m}], \quad (16)$$

where σ_τ^2 is the pseudorange variance, B_L is the loop bandwidth, d is the Early-minus-Late spacing, and T_{chip} is the duration of a signal chip. Note that Equation (16) is the formula obtained for a Delay Lock Loop (DLL) using a coherent discriminator. In our work, a normalized non-coherent Early-minus-Late envelope discriminator (Kaplan and Hegarty, 2005, p. 174) was used. For this type of DLL discriminator, an additional term including the so-called “squaring loss” should be accounted for. In this work, the effect of the squaring loss is neglected, and Equation (16) is used as approximation for the pseudorange variance. The effectiveness of Equation (16) is investigated in Figure 2 that shows the variance of pseudorange measurements as a function of the estimated C/N_0 . The empirical variances in Figure 2 have been estimated from real measurements generated using standard processing. In particular, the data collected during Test 1 described in Section 5.1 have been used. Third-order polynomials

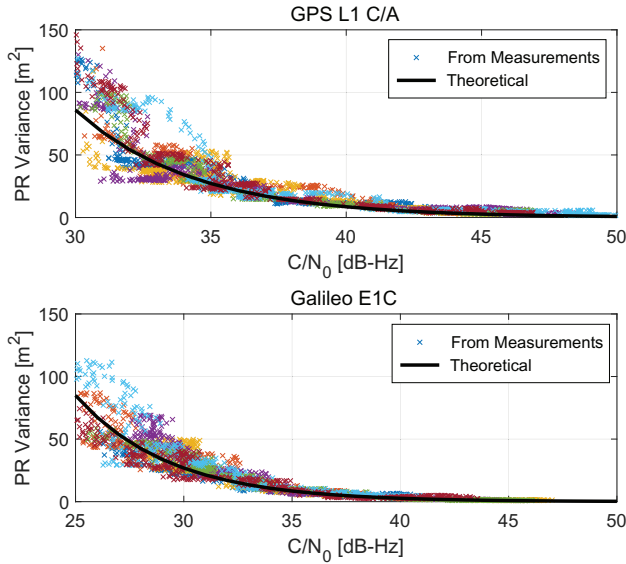


FIGURE 2 Variance of pseudorange measurements as a function of the estimated C/N_0 . Crosses represent variances estimated from the measurements obtained for Test 1; different colors indicate different satellites. Upper part: GPS L1 C/A measurements. Lower part: Galileo E1C measurements. [Color figure can be viewed in the online issue, which is available at wileyonlinelibrary.com and www.ion.org]

were used to remove the time-varying mean of the pseudoranges. These polynomials were fit to the data by considering analysis windows of 30 seconds. After mean removal, pseudoranges were used for the variance computation. The C/N_0 is the effective C/N_0 estimated by the receiver from the correlator outputs. Crosses of different colors in Figure 2 indicate that the variances were computed from different signals. The black solid line in Figure 2 is the theoretical curve shown in Equation (16). From the figure, it emerges that Equation (16) can be effectively used to determine the pseudorange variance from the signal C/N_0 . This result is valid for both GPS and Galileo signals that are considered in the two parts of Figure 2.

When interference mitigation is used, a reduction of effective C/N_0 is obtained and Equation (16) becomes

$$\sigma_{\tau, Mit}^2 \approx \frac{B_L d}{2L_o C/N_0} T_{chip}^2 \quad [\text{m}]. \quad (17)$$

Thus, a variance increase proportional to $1/L_o$ is expected on the pseudoranges.

If a WLS approach is used for the position computation, position updates are performed according to

$$\Delta \mathbf{x} = (H^T W H)^{-1} H^T W \mathbf{z} = G \mathbf{z}, \quad (18)$$

where $\Delta \mathbf{x}$ is the vector containing the state vector updates for the position and clock bias components. H is the design

matrix, and W is a weighting matrix. \mathbf{z} is the measurement vector containing the differences between actual and estimated pseudoranges (Kaplan & Hegarty, 2005). The matrix G is given by

$$G = (H^T W H)^{-1} H^T W. \quad (19)$$

The variances of the elements of \mathbf{z} are given by Equations (16) and (17) and depend on the C/N_0 of each received signal. Moreover, it is possible to assume that the elements of \mathbf{z} are uncorrelated. Thus, the covariance matrix of \mathbf{z} is given by Kaplan and Hegarty (2005):

$$\Sigma_z = \begin{bmatrix} \sigma_{\tau,1}^2 & 0 & \cdots & 0 \\ 0 & \sigma_{\tau,2}^2 & \cdots & 0 \\ 0 & 0 & \cdots & 0 \\ \cdots & \cdots & \cdots & \cdots \\ 0 & 0 & \cdots & \sigma_{\tau,N_m}^2 \end{bmatrix}, \quad (20)$$

where a subscript has been added in order to denote quantities related to the different pseudorange measurements. N_m is the number of measurements available. Matrix Σ_z is obtained in the absence of interference mitigation, and the variances on its diagonal are computed using Equation (16). When interference mitigation is used, a loss is introduced, and Equation (17) should be used. For RIM techniques, the LoE is independent from the input C/N_0 (Borio, 2017a; Borio & Closas, 2018, 2019). This is also approximately true for the ANF (Borio et al., 2006). For this reason, the measurement covariance matrix becomes

$$\Sigma_z^{Mit} = \frac{1}{L_o} \Sigma_z, \quad (21)$$

where $\frac{1}{L_o}$ is a scalar term. Since state vector updates are related to the measurements by Equation (18), the covariance of the position updates is obtained through the propagation of variance formula (Strang & Borre, 1997, Sec 9.6):

$$\Sigma_x = G \Sigma_z G^T. \quad (22)$$

Thus, the effect of interference mitigation on the covariance of the position solution is given by

$$\Sigma_x^{Mit} = \frac{1}{L_o} G \Sigma_z G^T = \frac{1}{L_o} \Sigma_x. \quad (23)$$

Equation (23) indicates that an increase in the position variance equal to $1/L_o$ is expected. It is noted that L_o is usually quite reduced. For example, when the complex signum non-linearity is used (Borio & Closas, 2018),

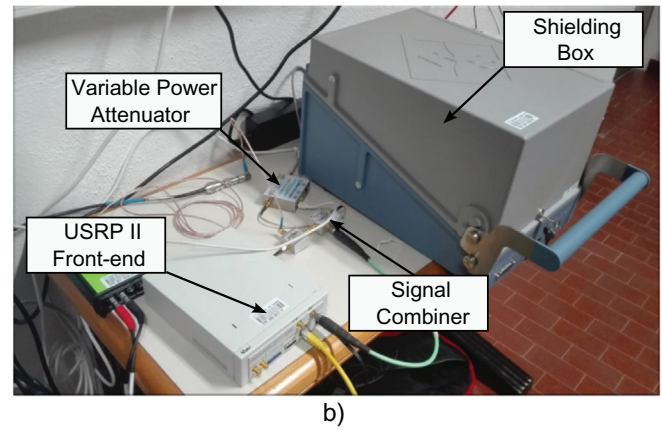
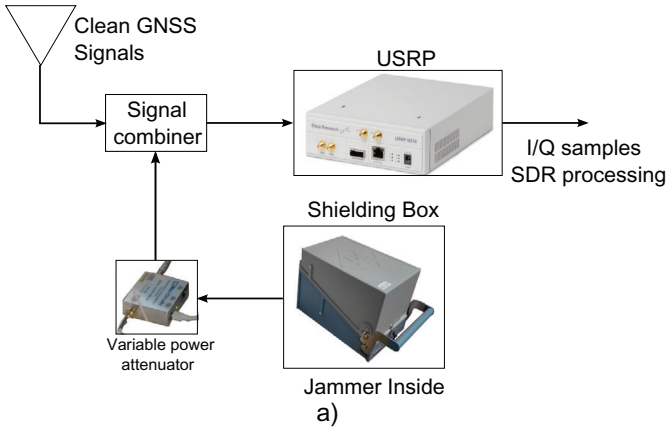


FIGURE 3 Experimental setup adopted to test the impact of robust jamming mitigation techniques on measurements and position solutions. a) Schematic representation of the setup. b) Actual view of one of the experiments involving Galileo E5b signals. [Color figure can be viewed in the online issue, which is available at wileyonlinelibrary.com and www.ion.org]

$$L_o = \frac{\pi}{4} = 0.7854. \quad (24)$$

This corresponds to an increase of position standard deviation equal to 1.128, which is less than 13%. This loss was obtained without taking into account front-end filtering and other imperfections. When these factors are accounted for, the LoE is further reduced. Results from real tests confirm this fact and show that the impact of RIM is lower than that theoretically expected.

5 | EXPERIMENTAL SETUP

In order to test the impact of the different interference mitigation techniques, several experiments were conducted. The tests differ for the jammer used, the type of quantization adopted, and the GNSS modulation considered. For all the tests, a dedicated experimental setup was developed. A jammer was placed inside a shielding box whose output was connected to a variable attenuator, adopted to generate different jamming power levels. The output of the variable attenuator was then combined with clean GNSS signals collected from a rooftop antenna. In this way, jammed GNSS signals were obtained. A USRP 2 was used to collect I/Q data that were then processed using a custom Matlab software receiver. A schematic representation of the experimental setup is provided in Figure 3a) whereas an actual view of the experimental setup is shown in Figure 3b). While additional hardware is visible in Figure 3b), it was not used for the data collections described in the following. For this reason, these additional components are not described.

The two jammers shown in Figure 4 were used for the three tests analyzed in the following. The first one shown

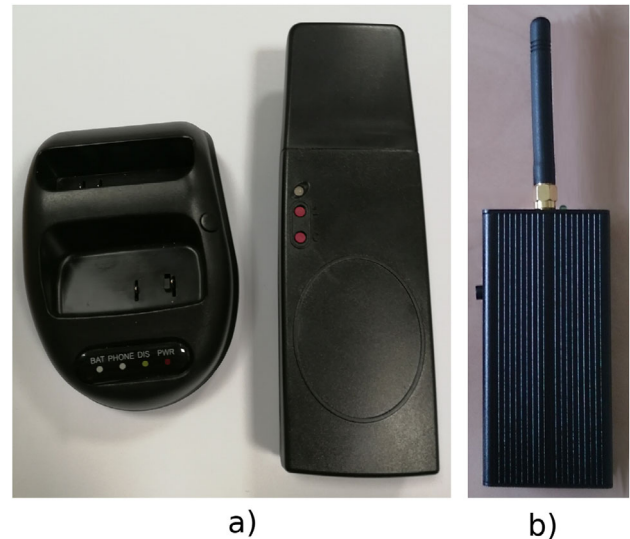


FIGURE 4 The two jammers used for the tests: a) Battery powered jammer in the shape of a cordless phone used for Test 1 and Test E5b. b) Battery powered jammer with SMA connector and detachable antenna used for Test 2. [Color figure can be viewed in the online issue, which is available at wileyonlinelibrary.com and www.ion.org]

in Figure 4a) was used for Test 1 and Test E5b, the experiment conducted to study the Galileo E5b signal. It is a battery powered jammer with integrated antenna and belongs to Group 3 of the classification proposed by Mitch et al. (2011). It has been designed to have the shape of a cordless phone and cannot be connected to an external antenna. It is able to broadcast swept signals on different GNSS frequency bands including GPS L1, GPS L2, and Galileo E5b. The second jammer shown in Figure 4b) is also battery power with a Sub-Miniature version A (SMA) antenna connector. For this reason, it belongs to Group 2 of the classification suggested by Mitch et al. (2011). The

TABLE 2 Parameters used for the different tests

Parameter	Test 1 Value	Test 2 Value	Test E5b Value
Sampling Frequency	10 MHz	10 MHz	25 MHz
Center Frequency	1575.42 MHz	1575.42 MHz	1207.14 MHz
Sampling Type	Complex, IQ	Complex, IQ	Complex, IQ
No. bits	8	16	8

characteristics of the signals broadcast by these jammers are better detailed in the following sections.

Three signals were considered: GPS L1 C/A signals, the BOC modulation adopted by Galileo E1b/c signals, and the wideband BPSK modulation adopted by the Galileo E5b component. For both Galileo E1b/c and E5b signals, pilot processing was implemented. Signals on the L1 frequency were collected with a 10 MHz sampling frequency, whereas Galileo E5b components were collected using a 25 MHz sampling frequency. The Galileo E5b is considered wideband, and the main lobe of its spectrum occupies most of the frequencies captured by the USRP. The custom software receiver generates RINEX files that were used for the measurement and position domain analysis. The same datasets have been processed using standard processing and the different interference mitigation techniques reviewed in Section 2.

The parameters used for the different tests are summarized in Table 2 whereas a detailed description of each experiment is provided in the following.

5.1 | GPS/Galileo L1 - Test 1

The first test focused on the Galileo E1 Open Service (OS) and GPS L1 C/A signals and was performed using the jammer shown in Figure 4a). The signal broadcast by this jammer in the L1 band has a sweep period of about $9.1 \mu\text{s}$ and spans a frequency range of about 36 MHz. This frequency range is significantly larger than the sampling frequency (10 MHz) used for this test, and for this reason, the jamming signal periodically enters and exits the USRP input band resulting in a sequence of pulses clearly visible in the lower spectrogram in Figure 5.

In the first test, the USRP was configured to collect samples using 8 bits for signal quantization. Signal quantization has a significant impact on the ability of a receiver to withstand and mitigate interference (Cutright et al., 2003; Hegarty, 2011). When a low number of bits is used for signal quantization, front-end saturation occurs at lower interference power levels. When the front-end saturates, nonlinear effects occur, and the impact of interference is worsened by the presence of harmonics and cross-terms. For this

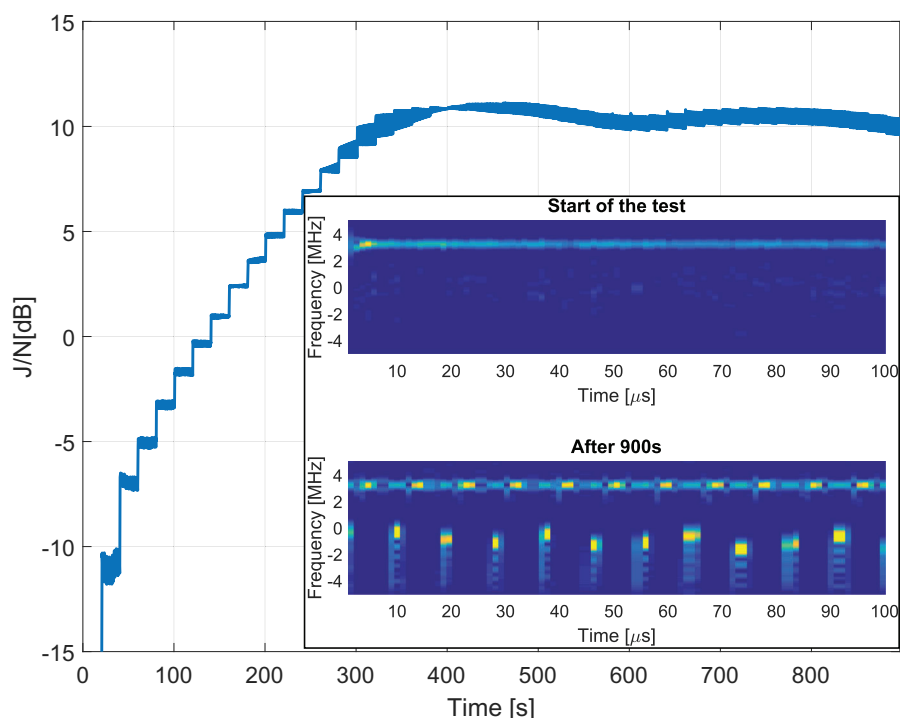


FIGURE 5 Estimated J/N profile of the first test conducted on the GPS/Galileo L1 frequencies. In the box: spectrograms of collected samples at the beginning of the test and after 900s. The zero frequency corresponds to 1575.42 MHz. After about 400 seconds from the start of the test, front-end saturation occurs, and the estimated J/N starts flattening out. [Color figure can be viewed in the online issue, which is available at wileyonlinelibrary.com and www.ion.org]

reason, tests with a different number of bits have been conducted.

The variable attenuator was configured in order to provide an initial attenuation equal to 70 dB. The attenuation was then decreased by 1 dB every 20 seconds. The J/N profile estimated from the collected samples is provided in Figure 5: in the first part of the experiment, the J/N progressively increases reflecting the attenuation steps. After about 400 seconds from the start of the experiment, the estimated J/N starts saturating, and the interference power does not increase significantly. This is due to the saturation of the front-end: the interference signal is mostly represented by the maximum and minimum levels of the front-end ADC. In this respect, the ADC quantization function clips the interference signal creating nonlinear effects.

The right bottom box of Figure 5 shows the spectrograms of the signals collected at the beginning of the test and after 900 seconds from the start of the experiment. At the beginning of the test, only an horizontal line can be observed in the spectrogram. This line corresponds to the clock harmonic generated by the USRP 2 front-end. After 900 seconds from the start of the experiment, the attenuation is at its minimum value (25 dB), and the jamming component dominates. In this case, periodic pulses appear in the spectrogram. It is also interesting to note that the spectral line corresponding to the clock component occupies a larger frequency band. In Borio and Gioia (2020), the Power Spectral Densities (PSD) of the jammed signal is provided, and it is shown that several harmonics are present around the clock terms. This effect is likely due to the interaction between the clock and jamming component. The ANF can hardly mitigate an interference signal with the characteristics shown in Figure 5.

5.2 | GPS/Galileo L1 - Test 2

A 16-bit quantization was adopted for the second test. In this case, the jammer shown in Figure 4b) was used. It broadcasts a swept signal with a period of about $6.3 \mu\text{s}$ and with a sweep range of about 20.3 MHz. Also, in this case, the jamming signal spans a frequency range significantly larger than the front-end input frequency band and is perceived by the receiver as a sequence of pulses. The impulsive nature of the received jamming signal is due to the fact that it periodically enters and exits the receiver input band: when outside such band, it is filtered out leading to clean GNSS signals. When inside, a strong interference pulse is observed.

The initial attenuation applied to the jamming signal was set to 50 dB and progressively reduced every 30 sec-

onds with a 1 dB step. The minimum attenuation was equal to 25 dB. In this way, the J/N profile shown in Figure 6 was obtained. Also, in this case, saturation effects can be clearly seen, and two working regions can be distinguished. In the first part of the test, the estimated J/N reflects the attenuation profile described above. After about 500 seconds from the start of the experiment, the receiver front-end starts saturating, and the J/N reaches an almost constant value.

As for the previous test, the bottom right box of Figure 6 shows the spectrograms of the input samples at the beginning of the experiment and after 500 seconds. The spectrogram of the samples collected at the beginning of the experiment does not show any specific feature and reflects the absence of interference. The second spectrogram is characterized by significantly higher power levels. While some dark blue areas are still present, indicating the fact that the jamming signal is exiting the front-end band, most of the spectrogram is cluttered by interference power. The jammer signal is wideband, and nonlinear effects, due to saturation, further spread its energy over the time-frequency plane.

5.3 | Galileo E5b

The Galileo E5b signal is finally considered in this third test. As for Test 1, the jammer shown in Figure 4a) was used: the signal component broadcast in the E5b frequency band is also swept with a period of about $9.1 \mu\text{s}$. While its sweep range (about 45.7 MHz) is significantly larger than the input receiver band, its frequency pattern is such that the signal spends most of the time inside the front-end input frequency range. For this reason, a clear frequency pattern can be observed in the lower spectrogram of Figure 7.

The attenuation profile started at 70 dB and was progressively decreased to a minimum of 20 dB. At this point, it was kept constant for two minutes and increased again. The attenuation was decreased by steps of 0.25 dB each two seconds (1.25 dB each ten seconds). These settings led to the J/N profile shown in Figure 7. Note that in this case, smaller steps were used for the generation of the J/N profile with respect to the previous two test cases. When a step-wise power profile is used, the receiver may lose lock in correspondence of the power step/transition. A smoother jamming profile was selected here in order to test different stress conditions on the receiver. In this case, a 8-bit quantization was adopted.

The spectrograms provided in the bottom right box of Figure 7 provide a time-frequency representation of the signal conditions at the start of the experiment and after 500 seconds. As for the previous cases, the spectrogram obtained at the beginning of the test does not reveal any

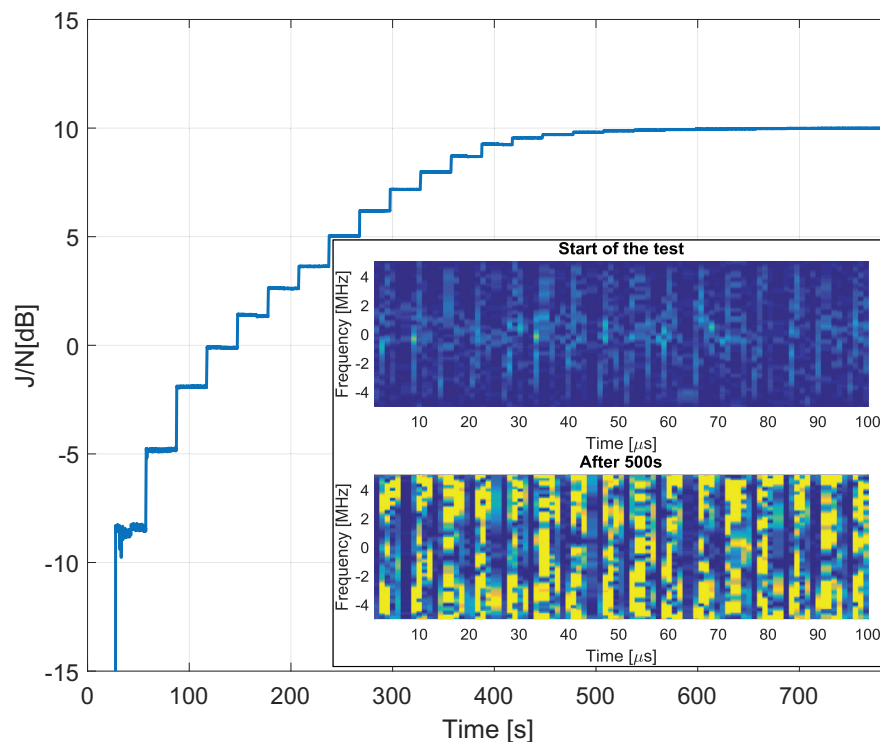


FIGURE 6 J/N profile estimated for the second test conducted on the GPS/Galileo L1 frequencies. In the box: spectrograms of collected samples at the beginning of the test and after 500s. The zero frequency corresponds to 1575.42 MHz. After about 500 seconds from the start of the test, front-end saturation occurs, and the estimated J/N starts flattening out. [Color figure can be viewed in the online issue, which is available at wileyonlinelibrary.com and www.ion.org]

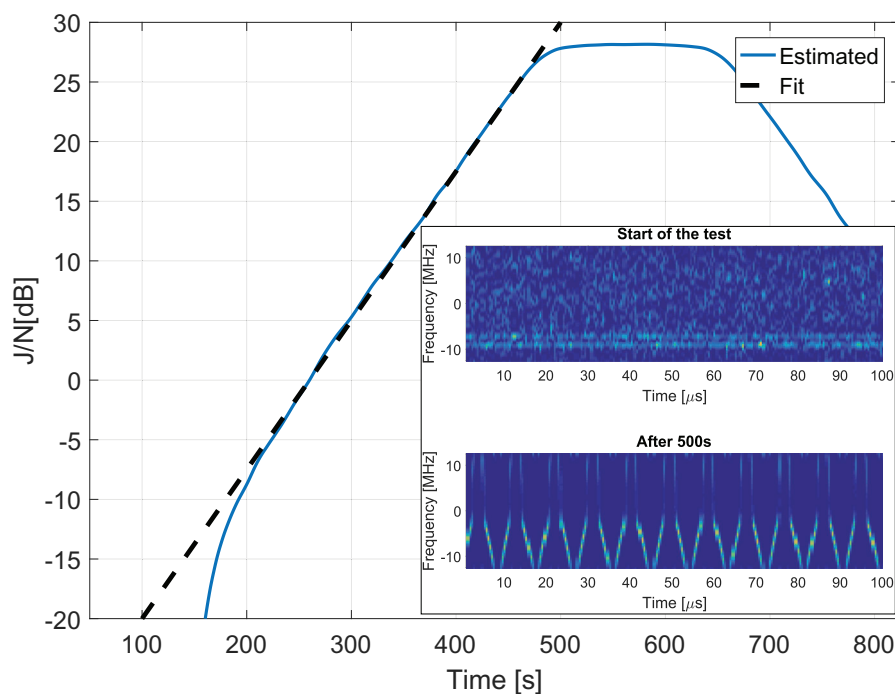


FIGURE 7 J/N profile estimated for one of the experiments conducted in the Galileo E5B band. In the box: spectrograms of collected samples at the beginning of the test and after 500s. The zero frequency corresponds to 1207.14 MHz. After 500 seconds from the start of the test, a minimum attenuation equal to 20 dB was obtained. This attenuation is kept constant for two minutes and increased again. [Color figure can be viewed in the online issue, which is available at wileyonlinelibrary.com and www.ion.org]

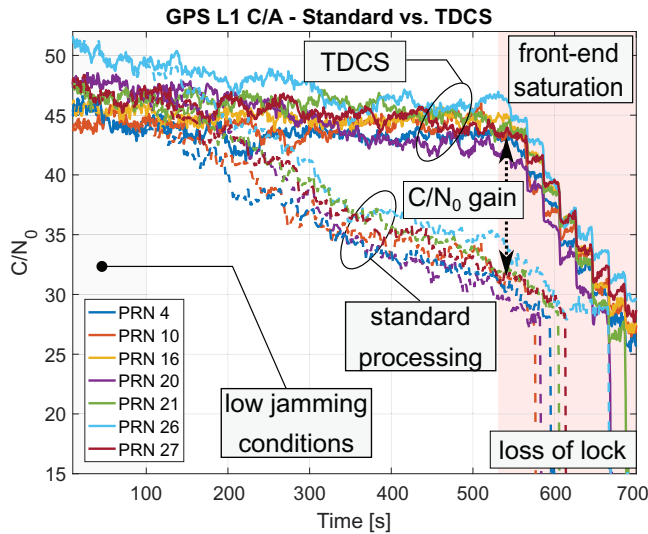


FIGURE 8 Comparison between C/N_0 time series obtained without mitigation and using the TDCS approach for Test 1. Dashed lines refer to C/N_0 values obtained using standard processing without mitigation. GPS L1 C/A signals. [Color figure can be viewed in the online issue, which is available at wileyonlinelibrary.com and www.ion.org]

specific features apart from two faint horizontal lines, which correspond to clock harmonics. In the second spectrogram, clear swept components corresponding to the jamming signal can be observed.

6 | EXPERIMENTAL RESULTS

6.1 | Test 1

Interference mitigation techniques can significantly enhance the performance of GNSS receivers. The benefits of such techniques are particularly evident when considering acquisition and tracking results. Figure 8 compares C/N_0 time series obtained without mitigation and using the TDCS approach, one of the techniques leading to the best results for the processing of the data collected under Test 1. The C/N_0 is estimated at the tracking level and reflects the signal quality and the receiver ability to track signals. In this respect, the estimated C/N_0 can be used as a loss-of-lock indicator (Van Dierendonck, 1996).

During the first part of Test 1, the jamming power can be neglected, and the impact of mitigation techniques is assessed under interference-free conditions. The C/N_0 time series obtained with and without mitigation coincide for the first 100 seconds of the test. This shows that the LoE introduced by the TDCS is lower than the theoretical value (about 1 dB) expected for this type of technique. This result was discussed in Section 4, and it is confirmed here

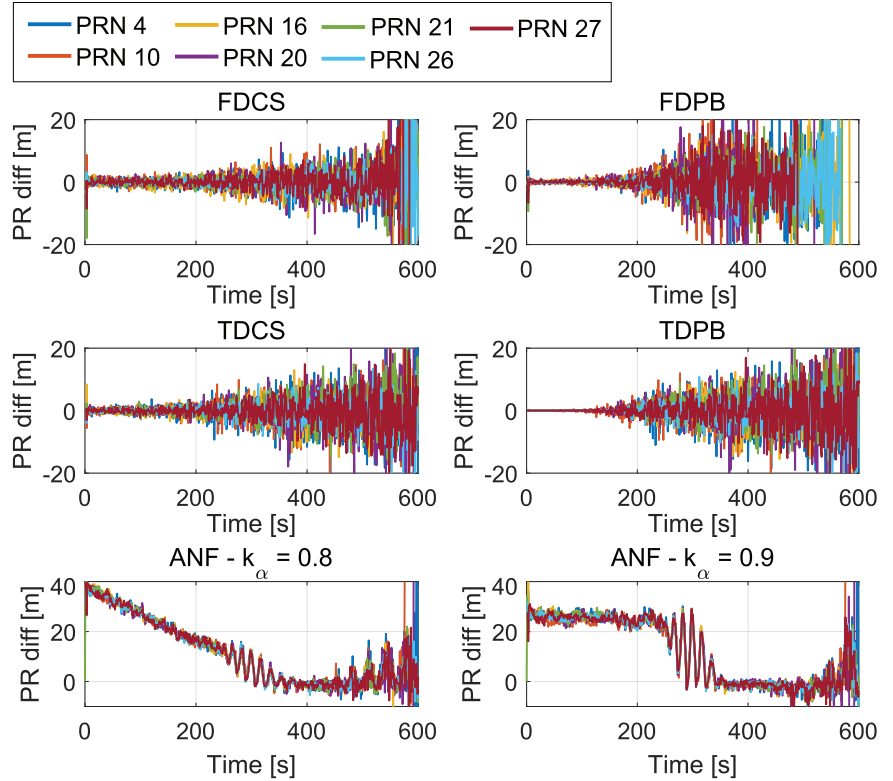
by experimental results. After about 100 seconds, the C/N_0 estimated without interference mitigation starts decreasing whereas the C/N_0 obtained using the TDCS is only marginally influenced by the jamming component. After about 500 seconds from the start of the test, TDCS provides a C/N_0 gain of about 15 dB. At this point of the experiment, saturation effects start playing a significant role, and also the TDCS is affected. As the jamming power is further increased, non linear saturation effects worsen and reduce TDCS performance. When the receiver front-end is fully saturated, no mitigation is possible. While every interference mitigation technique has limitations, the benefits of such approaches are clearly shown in Figure 8. The TDCS approach prevents early loss-of-locks and provides better position and measurement availability. In the following, a position solution is declared unavailable when less than four satellite signals are tracked. For example, in Figure 8, standard processing is unable to provide a position solution when lock is lost on signal Pseudo-Random Noise (PRN) 4 at about 595 seconds from the start of the experiment.

Note that not all the interference mitigation techniques provide benefits with respect to standard processing. The final result depends on the type of jamming signal and on the parameters selected for the specific technique. In Test 1, the jamming signal is perceived as a sequence of pulses, which are effectively mitigated by time-domain techniques. Frequency domain approaches are less effective and can introduce degradations as better highlighted in the following.

The analysis of the five interference mitigation techniques at the signal processing level is out of the scope of this paper, and Figure 8 has been provided as a sample result. For this reason, the C/N_0 time series are not further analyzed in the following. Additional results on interference mitigation at the signal processing level can be found, for example, in Raasakka and Orejas (2014); Qin, Troglia Gamba, et al. (2019); Wendel et al. (2016); and Borio and Closas (2018).

Pseudorange differences between standard measurements and the observations from the five interference mitigation techniques considered in this work are shown in Figure 9 for the GPS L1 C/A signals collected during Test 1. Two types of behavior emerge from the figure: for RIM techniques, the pseudorange differences are zero mean, and no particular trends can be observed. In Borio and Closas (2018, 2019) and Borio (2017a), it was shown that RIM techniques do not introduce biases on the location of the main peak of the CAF. The CAF is in turn used for the computation of the pseudoranges. The lack of biases in the pseudorange differences reported in Figure 9 supports this theoretical result on RIM techniques. During the first 250 seconds of Test 1, the J/N is less than 7 dB (see Figure 5), and the jamming component can be neglected. In

FIGURE 9 Pseudorange differences between standard measurements and observations from the five interference mitigation techniques. The ANF has been tested for two values of k_α , the pole contraction factor. Test 1, GPS L1 C/A. [Color figure can be viewed in the online issue, which is available at wileyonlinelibrary.com and www.ion.org]



this part of the test, RIM techniques lead to pseudorange differences below 1 m, that is within the receiver processing noise. The RIM technique leading to the lowest differences is TDPB. As discussed in Section 2.3, the decision threshold was set to three times the total sample standard deviation estimated in the absence of interference. For this reason, for low J/N values, only a few samples are set to zero with extremely reduced pseudorange differences. With the increase of the J/N , pseudorange differences start diverging: this is the effect of jamming that is not mitigated in the standard measurements that are used to form the pseudorange differences.

The ANF acts differently, and a bias is introduced on the pseudoranges. This result was expected since notch filters are known to introduce additional delays on the measurements (Di Grazia et al., 2019; Giordanengo, 2009; Qin, Troglia Gamba, et al., 2019; Raasakka & Orejas, 2014). The bias introduced by the ANF is time-varying and depends on the jamming signal. As the jamming power increases, the adaptation algorithm of the ANF converges to different solutions leading to different delays. In Figure 9, the ANF has been tested for two values of its pole contraction factor: $k_\alpha = 0.8$ and $k_\alpha = 0.9$. While higher delays are experienced for $k_\alpha = 0.8$, similar behaviors are observed in the two cases: most of the delays introduced by the ANF are common to all the pseudoranges. While small inter-measurement biases are expected, due to the different Doppler frequencies of the signals, these delays are

within the processing noise of a SPP solution. Additional analysis is required to assess the impact of the ANF on carrier phase-based position solutions.

The pseudorange differences obtained for the Galileo E1c signals are shown in Figure 10. Also, in this case, the pseudorange differences obtained using RIM techniques are zero mean, and no clear biases can be identified. The ANF introduces time-varying biases for both $k_\alpha = 0.8$ and $k_\alpha = 0.9$. The biases are, however, different from those observed in Figure 9 for the GPS L1 C/A signals. This result depends on the fact that GPS L1 C/A signals and the Galileo E1c components have different spectral characteristics determined by their specific modulations, a BPSK and a BOC, respectively. Thus, the spectra of the two signals are affected differently by the ANF. As already mentioned, the time-varying nature of the delay introduced by the ANF is due to the jamming power that is progressively increased during the experiment.

Position errors are analyzed in Figure 11 for the GPS L1 case. Since the two ANF cases evaluated above were leading to similar results, only $k_\alpha = 0.8$ is considered here. The position errors obtained for the five interference mitigation techniques follow the same trend observed for the standard case without indicating the presence of biases. This is also true for the ANF, which does not introduce noticeable biases in the SPP solution. Shaded areas in Figure 11 indicate the portion of the test where the jamming power is negligible: here, all the time series coincide showing that

FIGURE 10 Pseudorange differences between standard measurements and observations from the five interference mitigation techniques. The ANF has been tested for two values of k_α , the pole contraction factor. Test 1, Galileo E1c. [Color figure can be viewed in the online issue, which is available at wileyonlinelibrary.com and www.ion.org]

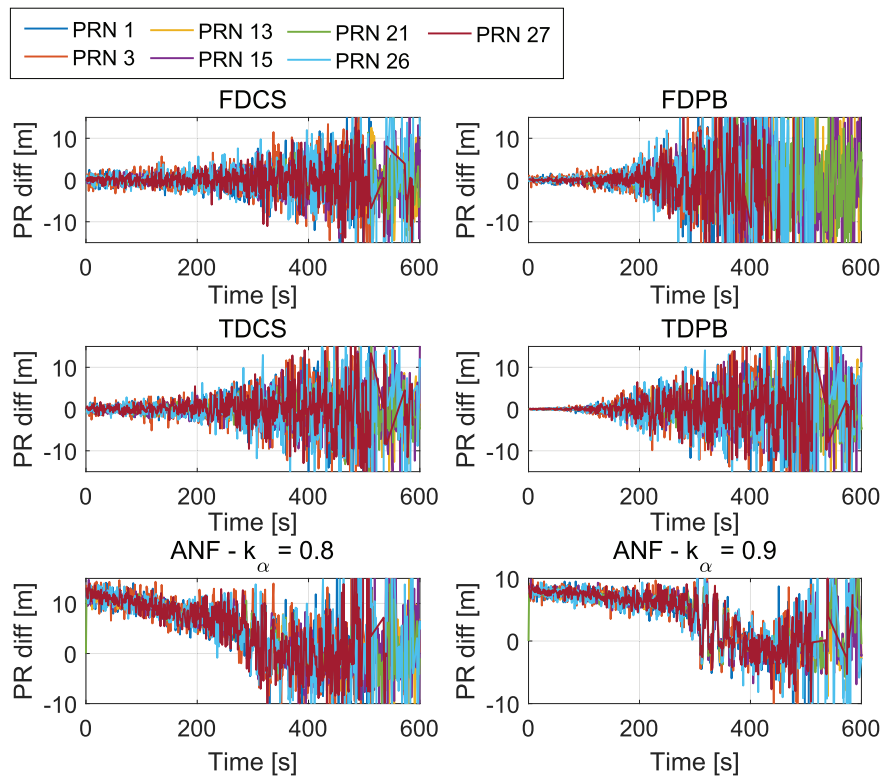
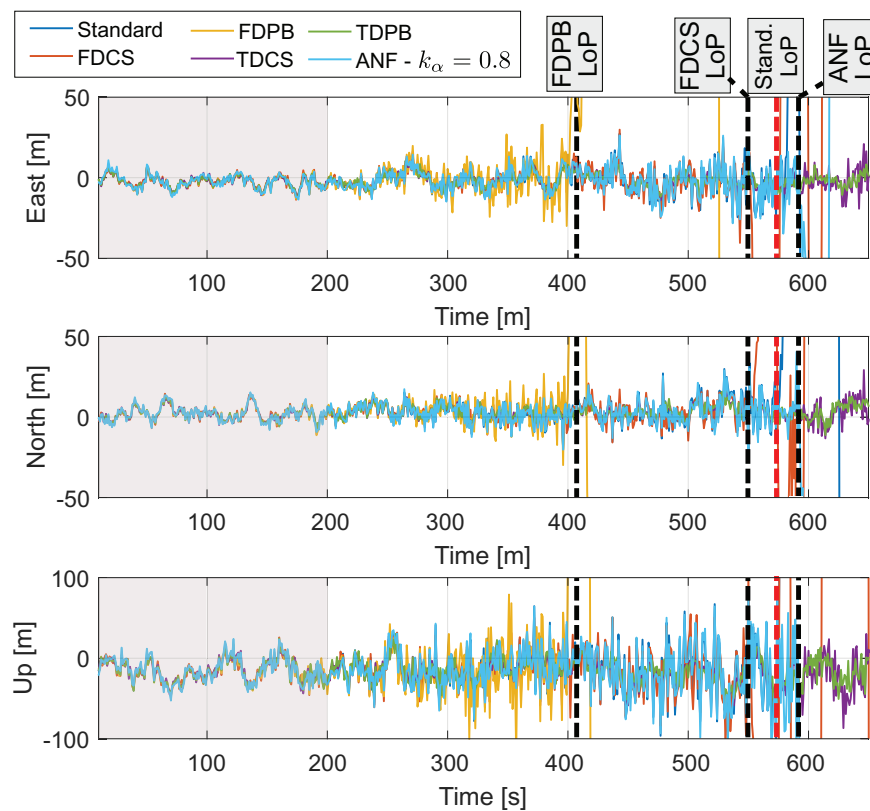


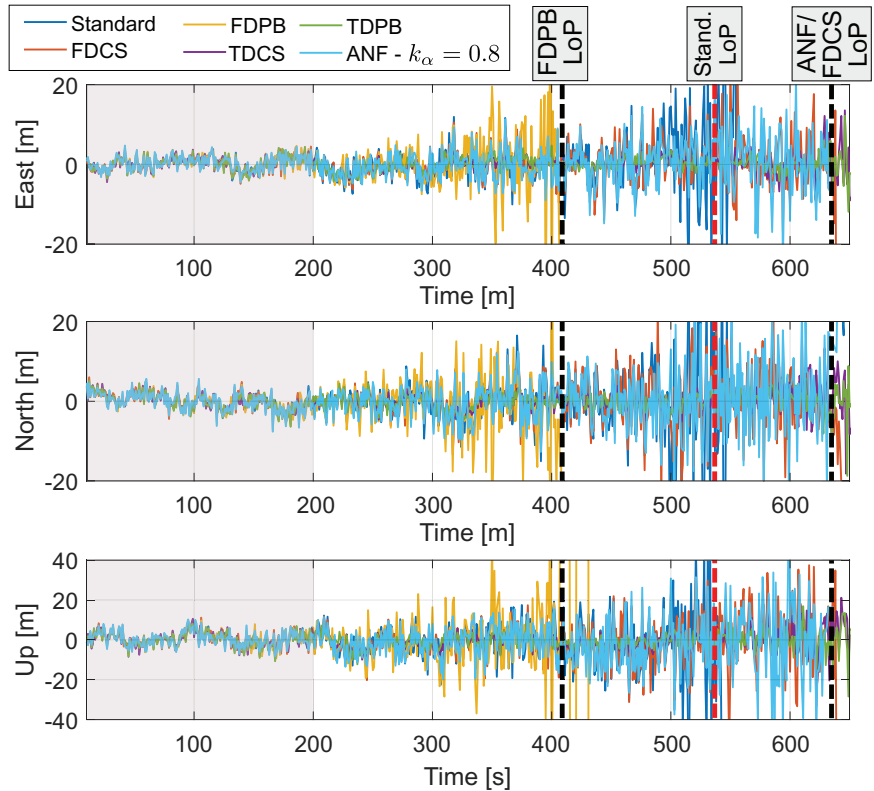
FIGURE 11 Position errors in the ENU frame. Comparison between different interference mitigation techniques for GPS L1 C/A only positioning. The shaded areas indicate the portion of the test where jamming can be neglected. Test 1, 8 bits. “LoP” is used to indicate loss of position solution. [Color figure can be viewed in the online issue, which is available at wileyonlinelibrary.com and www.ion.org]



interference mitigation techniques do not degrade receiver performance in the absence of interference. In this respect, the LoE can be considered negligible as discussed in Section 4.

The figure also shows when the position solution is no longer available for a specific technique: in this case, FDPB leads to the worst performance. Indeed, for high levels of interference, its position solutions become noisier than

FIGURE 12 Position errors in the ENU frame. Comparison between different interference mitigation techniques for Galileo E1c only positioning. The shaded areas indicate the portion of the test where jamming can be neglected. Test 1, 8 bits. “LoP” is used to indicate loss of position solution. [Color figure can be viewed in the online issue, which is available at wileyonlinelibrary.com and www.ion.org]



those obtained without interference mitigation. Moreover, an early Loss of Position (LoP) occurs. This indicates that the spectral representation of the jamming signal is, in this case, not sparse in the frequency domain and that FDPB is removing an excessive number of frequency samples. The fact that the frequency representation of the jamming signal was not sufficiently sparse, is confirmed by the results obtained with FDCS that did not improve the receiver performance with respect to standard processing. On the contrary, time domain processing was quite effective and provided consistent position solutions even for high levels of receiver saturation. In this respect, both TDPB and TDCS provide position solutions until about 700 seconds from the start of the test, which correspond to significant levels of front-end saturation. The ANF did not significantly improve the receiver performance. This is mainly due to the impulsive nature of the specific jamming component as highlighted by the spectrograms provided in Figure 5.

The position errors obtained using a Galileo only solution are evaluated in Figure 12. The position solutions have been obtained using the pseudoranges analyzed in Figure 10. While the usage of Galileo E1c signals lead to more accurate position solutions, the time series provided in Figure 12 confirm the findings discussed above for the GPS L1 C/A modulation: no significant degradations are introduced by interference mitigation when low levels of jamming are present. Since in this case the jamming

component is concentrated in the time domain, frequency domain processing spreads the interference terms on a large number of frequency samples making frequency domain RIM ineffective.

Additional complementary results can be found in Borio and Gioia (2020).

6.2 | Test 2

In this section, sample results obtained for Test 2 are briefly presented. The test considered GPS/Galileo L1 signals with a 16-bit quantization. Pseudorange differences for the GPS L1 C/A case are provided in Figure 13: also, in this case, clear biases are visible only when the ANF is used with similar behaviors for $k_\alpha = 0.8$ and $k_\alpha = 0.9$. For low J/N values, RIM techniques lead to pseudorange differences in the meter level. These differences increase with time and reflect the impact of an increasing J/N . As for the previous case, FDPB is not effective, and this result reflects the fact that pulse interference is spread in the frequency domain leading to ineffective mitigation. This finding indicates the importance of selecting the proper domain for interference mitigation.

As for Test 1, the ANF introduces a delay that is a function of the jamming signal characteristics. Clear steps corresponding to the different jamming power levels can be observed in the two ANF boxes of Figure 13. These

FIGURE 13 Pseudorange differences between standard measurements and observations from the five interference mitigation techniques. The ANF has been tested for two values of k_α , the pole contraction factor. Test 2, GPS L1 C/A. [Color figure can be viewed in the online issue, which is available at wileyonlinelibrary.com and www.ion.org]

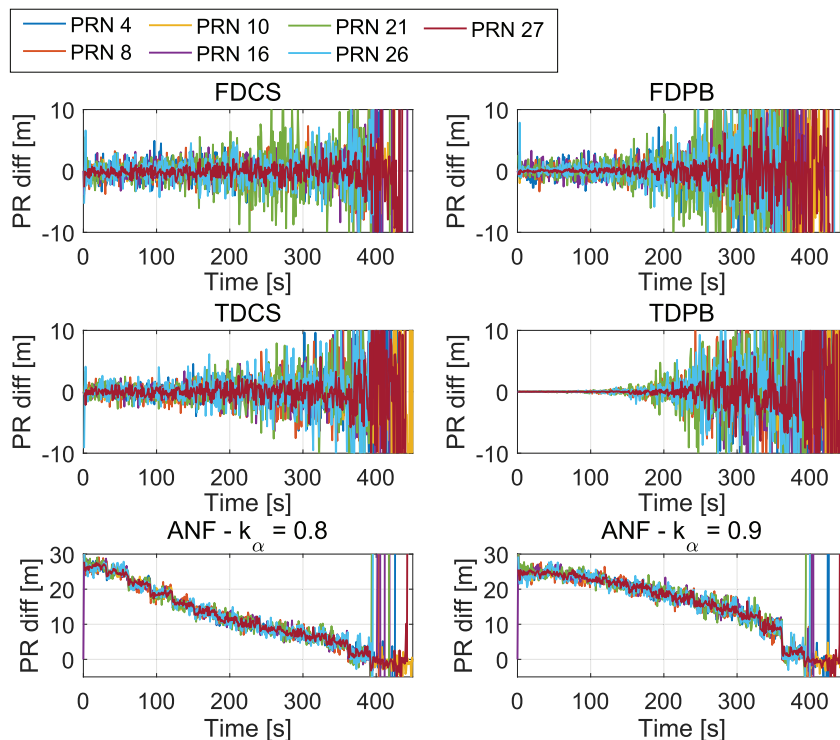
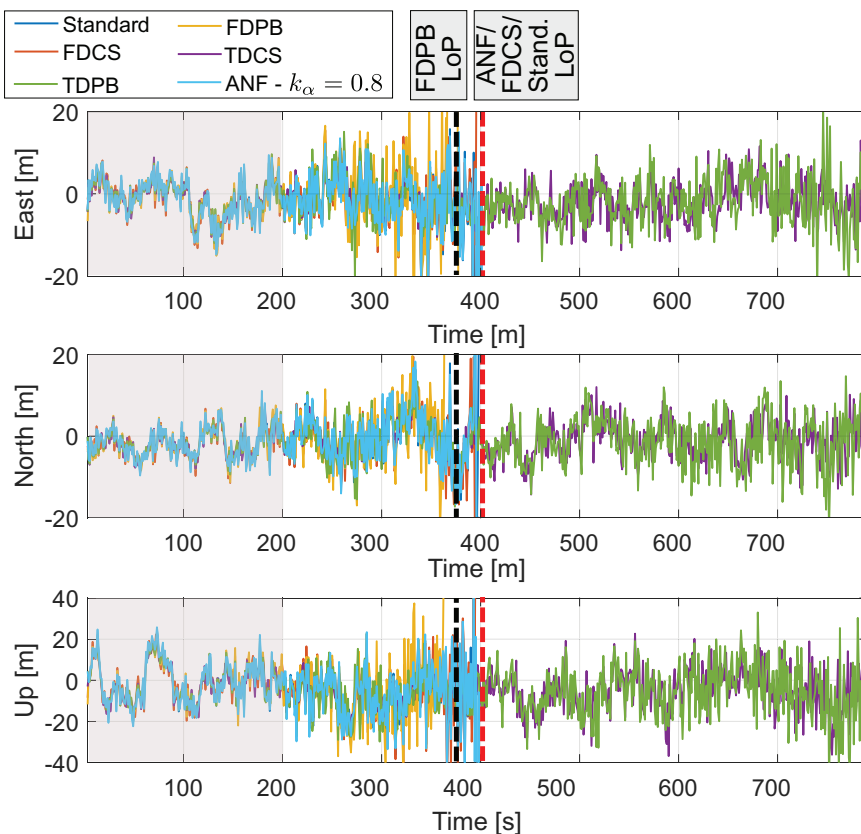


FIGURE 14 Position errors in the ENU frame. Comparison between different interference mitigation techniques for GPS L1 C/A only positioning. The shaded areas indicate the portion of the test where jamming can be neglected. Test 2, 16 bits. “LoP” is used to indicate loss of position solution. [Color figure can be viewed in the online issue, which is available at wileyonlinelibrary.com and www.ion.org]

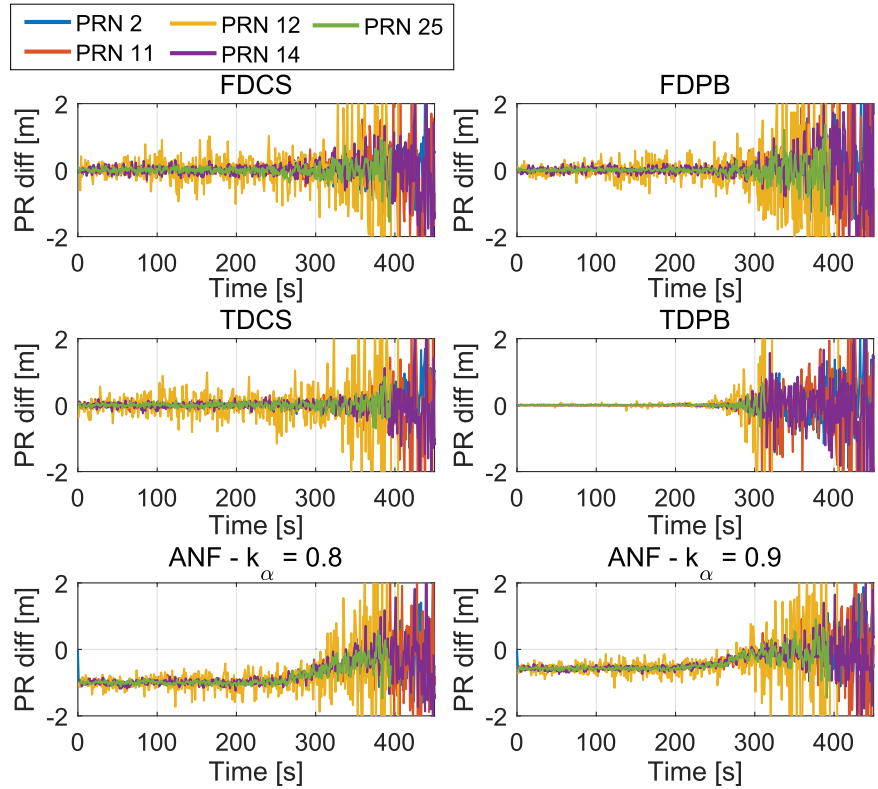


results are also valid for the Galileo case that is not explicitly analyzed to avoid repetition of similar results.

The position errors in the ENU frame are analyzed in Figure 14 for the GPS L1 C/A only solution. The time

series reported in Figure 14 confirm the fact that the five interference mitigation techniques under investigation do not introduce biases. As for Test 1, most of the biases introduced by the ANF are common to all the measurements

FIGURE 15 Pseudorange differences between standard measurements and observations obtained using interference mitigation techniques. The ANF has been tested for two values of k_α , the pole contraction factor. Galileo E5b experiment. [Color figure can be viewed in the online issue, which is available at wileyonlinelibrary.com and www.ion.org]



and no noticeable effects are visible in the SPP solution considered in Figure 14. From Figure 14, it emerges that time domain RIM is very effective in mitigating the type of jamming signal considered for Test 2. Both TDCS and TDPB provide valid position solutions for the whole duration of the test and for significant levels of front-end saturation.

Similar findings were obtained when analyzing the Galileo only position solution.

6.3 | Galileo E5b test

Results related to the test conducted on the Galileo E5b signal are briefly presented in this section. Pseudorange differences between standard measurements and observations from the five interference mitigation techniques are provided in Figure 15. As for the previous cases, pseudorange differences are zero mean when RIM techniques are used whereas a clear bias is observed for the ANF. In all cases, the variance of the pseudorange differences increases with time, and this effect is due to the fact that the J/N is also increasing. Apart from the ANF cases, the pseudorange differences are in the centimeter order for low J/N values. In the first part of the test, the bias introduced by the ANF is about a meter for $k_\alpha = 0.8$ and about 60 centimeters for $k_\alpha = 0.9$. In both cases, biases start decreasing to zero after about 300 seconds from the start of the exper-

iment. This result is due to the adaptation behavior of the ANF, and it is similar to the effects discussed in Section 6.1. At the beginning of the test, the impact of jamming is negligible, and the ANF places its notch around the two CWs clearly visible in the upper spectrogram in Figure 7 and due to the clock of the USRP. In this portion of the test, the notch frequency is stable over time, and the behavior of the ANF can be approximated with that of a non-adaptive filter. As k_α approaches 1, the transfer function of the ANF better approximates that of an all-pass filter: this justifies the fact that a smaller bias is observed for $k_\alpha = 0.9$.

After about 300 seconds from the start of the experiment, the jamming component starts to be significant, and the ANF tracks their variations. This behavior is highlighted in Figure 16a) that shows the PSDs of the signals at the input and output of the ANF. The PSD have been computed using samples collected after 400 seconds from the start of the experiment. The figure also shows the transfer function of the ANF.

Figure 16b) shows the spectrogram of the input samples and the frequency estimated by the ANF. The zero of the notch changes rapidly trying to follow the frequency variations of the jamming components. In this case, it is more difficult to predict the impact of the ANF on the measurements. However, the results in Figure 15 seem to suggest that lower biases are obtained when the frequency of the notch is varying in a rapid way on a large frequency range.

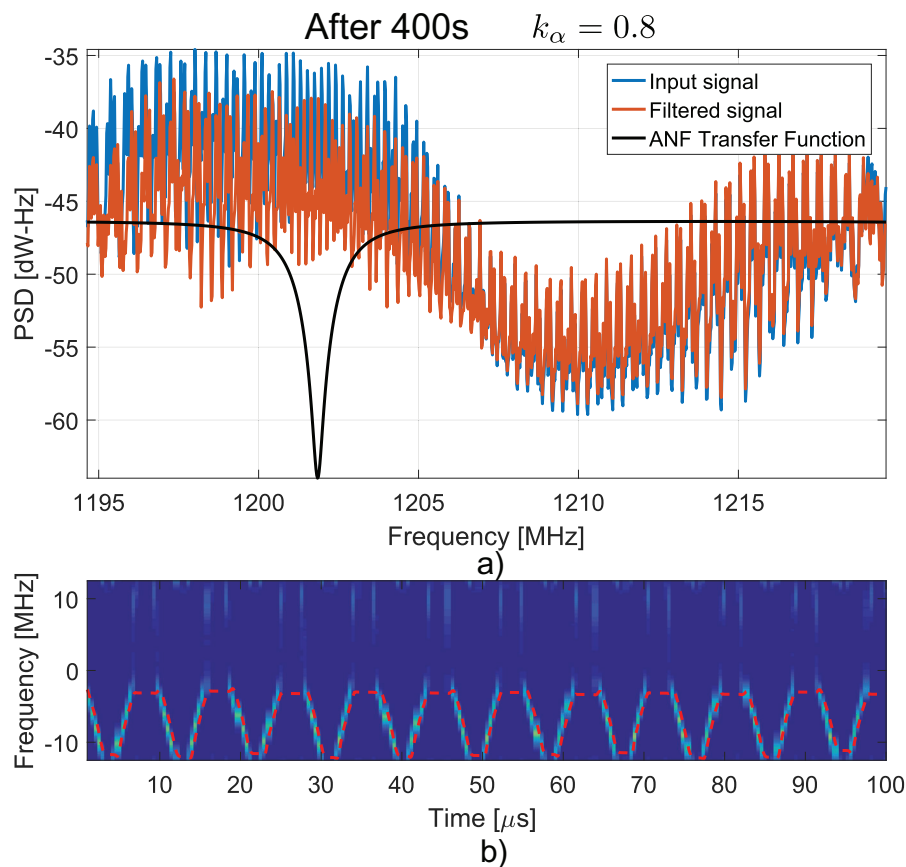
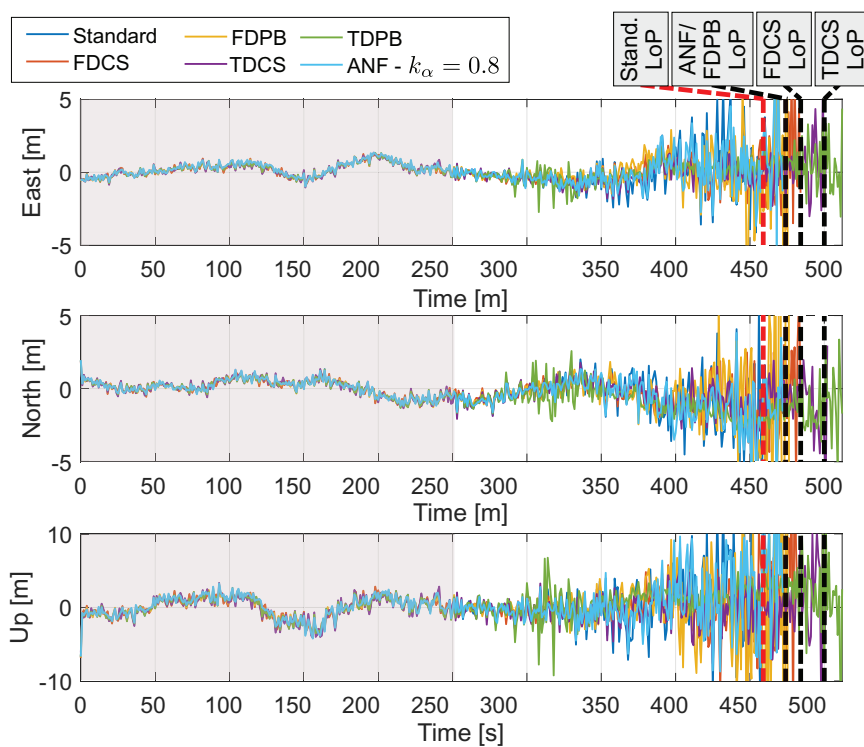


FIGURE 16 a) PSDs of the signals at the input and output of the ANF for $k_{\alpha} = 0.8$. The ANF transfer function is also provided. The transfer function of the ANF has been shifted in order to improve clarity. b) Spectrogram of the collected samples and frequency of the ANF notch (red dashed line). E5b test, samples collected after 400 seconds from the start of the experiment. [Color figure can be viewed in the online issue, which is available at wileyonlinelibrary.com and www.ion.org]

FIGURE 17 Position errors in the ENU frame. Comparison between different interference mitigation techniques for the Galileo E5b experiment. The shaded areas indicate the portion of the test where jamming can be neglected. “LoP” is used to indicate loss of position solution. [Color figure can be viewed in the online issue, which is available at wileyonlinelibrary.com and www.ion.org]



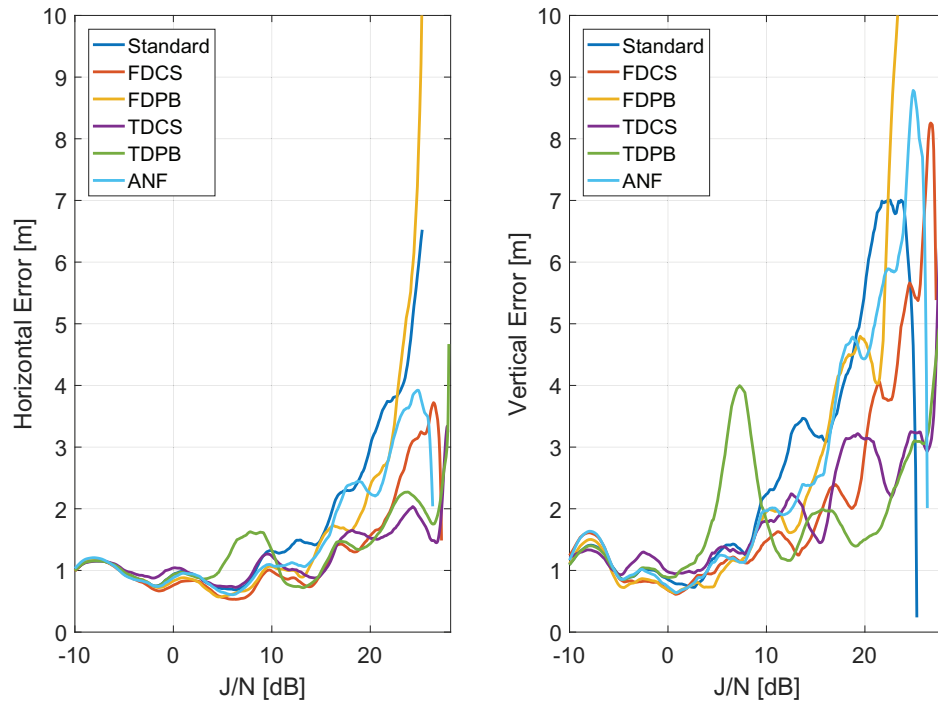


FIGURE 18 Position RMSE as a function of the estimated J/N . Left) Horizontal component Right) Vertical component. Comparison between different interference mitigation techniques for the Galileo E5b experiment. [Color figure can be viewed in the online issue, which is available at wileyonlinelibrary.com and www.ion.org]

As from the previous case, most of the bias introduced by the ANF is common to all pseudoranges. Thus, no biases are expected in the position solution. This fact is confirmed by the results shown in Figure 17, which provides position errors in the ENU frame. As for the previous cases, the position errors follow the same trend, and no significant differences can be observed between standard processing and interference mitigation techniques when low jamming power levels are experienced. In this case, TDCS and TDPB processing are the most effective techniques and lead to reasonable position solutions (vertical and horizontal errors within 5 m) for high levels of J/N . Also, the ANF provides some performance improvements with respect to standard processing. This is due to the fact that, in this case, the ANF is able to lock on the jamming component and track its variations as shown in Figure 16b).

Position performance is further investigated in Figure 18 that shows the horizontal and vertical position Root Mean Square Error (RMSE) as a function of the estimated J/N . The J/N is provided in Figure 7 whereas the average RMSE have been estimated using an analysis window of 30 seconds. The figure confirms the results discussed above and shows the benefits of using interference mitigation techniques.

7 | CONCLUSIONS

In this paper, five interference mitigation techniques were analyzed in the measurement and position domains, complementing results provided in previous studies that only considered their impact at the signal processing level. Different GNSS modulations were considered and several tests were conducted to experimentally characterize four RIM techniques. The ANF was used as a comparison term. From the analysis, it emerged that RIM techniques do not introduce biases at both measurement and position domains. Moreover, the degradations in terms of position error are negligible for low J/N levels. On the contrary, the ANF can introduce significant biases on the pseudoranges. These biases are difficult to predict, most of all when the ANF is tracking the fast frequency variations of a swept jamming signal. Most of these biases are, however, common to all the measurements and no noticeable effect was found in the final SPP solution.

In addition to this, it was shown that RIM can introduce a significant level of resilience with respect to jamming. This result is achieved when the processing domain is correctly selected along with the parameters of the RIM nonlinearities. In this respect, parameters improperly set could lead to performance degradations.

ORCID

Daniele Borio  <https://orcid.org/0000-0003-3573-5093>

Ciro Gioia  <https://orcid.org/0000-0001-6510-9240>

REFERENCES

- Bastide, F., Chatre, E., Macabiau, C., & Roturier, B. (2004, January). GPS L5 and GALILEO E5a/E5b signal-to-noise density ratio degradation due to DME/TACAN signals: Simulations and theoretical derivation. *Proceedings of the 2004 National Technical Meeting of The Institute of Navigation*, San Diego, CA, 1049–1062.
- Bastide, F., Macabiau, C., Akos, D. M., & Roturier, B. (2003, September). Assessment of L5 receiver performance in presence of interference using a realistic receiver simulator. *Proceedings of the 16th International Technical Meeting of the Satellite Division of The Institute of Navigation (ION GPS/GNSS 2003)*, Portland, OR, 142–152.
- Betz, J. W. (2000, January). Effect of narrowband interference on GPS code tracking accuracy. *Proceedings of the National Technical Meeting of The Institute of Navigation*, Anaheim, CA, 16–27.
- Betz, J. W. (2001, January). Effect of partial-band interference on receiver estimation of C/N_0 : Theory. *Proceedings of the National Technical Meeting of The Institute of Navigation*, Long Beach, CA, 817–828.
- Borio, D. (2017a). Myriad non-linearity for GNSS robust signal processing. *IET Radar Sonar and Navigation*, 11(10), 1467–1476. <https://doi.org/10.1049/iet-rsn.2016.0610>
- Borio, D. (2017b, May). Robust signal processing for GNSS. *Proceedings of the 2017 European Navigation Conference (ENC)*, Lausanne, Switzerland, 150–158. <https://doi.org/10.1109/EURONAV.2017.7954204>
- Borio, D., Camoriano, L., & Lo Presti, L. (2008). Two-pole and multi-pole notch filters: A computationally effective solution for GNSS interference detection and mitigation. *IEEE Systems Journal*, 2(1), 38–47. <https://doi.org/10.1109/JSYST.2007.914780>
- Borio, D., Camoriano, L., & Mulassano, P. (2006, September). Analysis of the one-pole notch filter for interference mitigation: Wiener solution and loss estimations. *Proceedings of the 19th International Technical Meeting of the Satellite Division of The Institute of Navigation (ION GNSS 2006)*, Fort Worth, TX, 1849–1860.
- Borio, D., & Cano, E. (2013). Optimal Global Navigation Satellite System pulse blanking in the presence of signal quantisation. *IET Signal Processing*, 7(5), 400–410. <https://doi.org/10.1049/iet-spr.2012.0199>
- Borio, D., & Closas, P. (2018). Complex signum non-linearity for robust GNSS signal processing. *IET Radar Sonar and Navigation*, 12(8), 900–909. <https://doi.org/10.1049/iet-rsn.2017.0552>
- Borio, D., & Closas, P. (2019). Robust transform domain signal processing for GNSS. *NAVIGATION*, 66(2), 305–323. <https://doi.org/10.1002/navi.300>
- Borio, D., Dovis, F., Kuusniemi, H., & Presti, L. L. (2016). Impact and detection of GNSS jammers on consumer grade satellite navigation receivers. *Proceedings of the IEEE*, 104(6), 1233–1245. <https://doi.org/10.1109/JPROC.2016.2543266>
- Borio, D., & Gioia, C. (2020, January). Robust interference mitigation: A measurement and position domain assessment. *Proceedings of the 2020 International Technical Meeting of The Institute of Navigation*, San Diego, CA, 274–288. <https://doi.org/10.33012/2020.1714>
- Borio, D., O'Driscoll, C., & Fortuny, J. (2012, December). GNSS jammers: Effects and countermeasures. *Proceedings of the 6th ESA Workshop on Satellite Navigation Technologies and European Workshop on GNSS Signals and Signal Processing*, Noordwijk, Netherlands, 1–7. <https://doi.org/10.1109/NAVITEC.2012.6423048>
- Calmettes, V., Pradeilles, F., & Bousquet, M. (2001, September). Study and comparison of interference mitigation techniques for GPS receiver. *Proceedings of the 14th International Technical Meeting of the Satellite Division of The Institute of Navigation (ION GPS)*, Salt Lake City, UT, 957–968.
- Cutright, C., Burns, J. R., & Braasch, M. (2003, June). Characterization of narrow-band interference mitigation performance versus quantization error in software radios. *Proceedings of the 59th Annual Meeting of The Institute of Navigation and CIGTF 22nd Guidance Test Symposium*, Albuquerque, NM, 323–332.
- De Wilde, W., Sleewaegen, J. M., Bougard, B., & Van Hees, J. (2015, September). Advanced interference detection and mitigation in Septentrio's high precision receivers. *Proceedings of the 28th International Technical Meeting of the Satellite Division of The Institute of Navigation (ION GNSS+ 2015)*, Tampa, FL, 1656–1683.
- Di Grazia, D., Cardineau, D., & Pisoni, F. (2019, September). A NAVIC enabled hardware receiver for the Indian mass market. *Proceedings of the 32nd International Technical Meeting of the Satellite Division of The Institute of Navigation (ION GNSS+ 2019)*, Miami, FL, 189–199. <https://doi.org/10.33012/2019.16979>
- Gao, G. X., Heng, L., Hornbostel, A., Denks, H., Meurer, M., Walter, T., & Enge, P. (2013). DME/TACAN interference mitigation for GNSS: Algorithms and flight test results. *GPS Solutions*, 17, 561–573. <https://doi.org/10.1007/s10291-012-0301-9>
- Gao, G. X., Sgammini, M., Lu, M., & Kubo, N. (2016). Protecting GNSS receivers from jamming and interference. *Proceedings of the IEEE*, 104(6), 1327–1338. <https://doi.org/10.1109/JPROC.2016.2525938>
- Gevargiz, J., Rosenmann, M., Das, P., & Milstein, L. B. (1984, October). A comparison of weighted and non-weighted transform domain processing systems for narrowband interference excision. *IEEE Military Communications Conference*, Los Angeles, CA, 474–477. <https://doi.org/10.1109/MILCOM.1984.4794896>
- Gioia, C. (2014). *GNSS Navigation in difficult environments: Hybridization and reliability* (Doctoral dissertation, University Parthenope of Naples, Naples, Italy). https://pang.uniparthenope.it/sites/default/files/PhD_thesis.CG.pdf
- Gioia, C., & Borio, D. (2016). A statistical characterization of the Galileo-to-GPS inter-system bias. *Journal of Geodesy*, 90(11), 1279–1291. <https://doi.org/10.1007/s00190-016-0925-6>
- Giordanengo, G. (2009). *Impact of Notch Filtering on Tracking Loops for GNSS Applications* (Doctoral dissertation, Politecnico di Torino, Torino, Italy). https://schulich.ucalgary.ca/labs/position-location-and-navigation/files/position-location-and-navigation/giordanengo2009_phd.pdf
- Hegarty, C. J. (2011). Analytical model for GNSS receiver implementation losses. *NAVIGATION*, 58(1), 29–44. <https://doi.org/10.1002/j.2161-4296.2011.tb01790.x>
- Hegarty, C., Van Dierendonck, A. J., Bobyn, D., Tran, M., & Grabowski, J. (2000, June). Suppression of pulsed interference through blanking. *Proceedings of the IAIN World Congress and the 56th Annual Meeting of The Institute of Navigation*, San Diego, CA, 399–408.
- Hoffmann-Wellenhof, B., Lichtenegger, H., & Collins, J. (1992). *Global positioning system: Theory and practice*. Springer.
- Huber, P. J. (1964). Robust estimation of a location parameter. *Annals of Mathematical Statistics*, 35(1), 73–101. <https://doi.org/10.1214/aoms/1177703732>

- Huber, P. J., & Ronchetti, E. M. (2009). *Robust statistics* (2nd ed.). Wiley.
- Ioannides, R.T., Pany, T., & Gibbons, G. (2016). Known vulnerabilities of global navigation satellite systems, status, and potential mitigation techniques. *Proceedings of the IEEE*, 104(6), 1174–1194. <https://doi.org/10.1109/JPROC.2016.2535898>
- Kaplan, E. D., & Hegarty, C. (Eds.). (2005). *Understanding GPS: Principles and applications* (2nd ed.). Artech House Publishers.
- Kuusniemi, H. (2005). *User-level reliability and quality monitoring in satellite-based personal navigation* (Doctoral dissertation, Tampere University of Technology, Tampere, Finland). https://www.ucalgary.ca/engo_webdocs/other/Dissertation_Heidi_Kuusniemi_Sep05.pdf
- Medina, D., Li, H., Vilà-Valls, J., & Closas, P. (2019). Robust statistics for GNSS positioning under harsh conditions: A useful tool? *Sensors*, 19(24), 5402. <https://doi.org/10.3390/s19245402>
- Misra, P., & Enge, P. (2006). *Global positioning system: Signals, measurements, and performance* (2nd ed.). Ganga-Jamuna Press.
- Mitch, R. H., Dougherty, R. C., Psiaki, M. L., Powell, S. P., O'Hanlon, B. W., Bhatti, J. A., & Humphreys, T.E. (2011, September). Signal characteristics of civil GPS jammers. *Proceedings of the 24th International Technical Meeting of the Satellite Division of The Institute of Navigation (ION GNSS 2011)*, Portland, OR, 1907–1919.
- Musemeci, L., & Dovis, F. (2015a). Interference mitigation based on transformed domain techniques. In F. Dovis (Ed.), *GNSS interference threats and countermeasures* (pp. 149–178). Artech House.
- Musemeci, L., & Dovis, F. (2015b). Classical digital signal processing countermeasures to interference in GNSS. In F. Dovis (Ed.), *GNSS interference threats and countermeasures* (pp. 127–148). Artech House.
- Pattinson, M., Lee, S., Bhuiyan, Z., Thombre, S., Manikundalam, V., & Hill, S. (2017). STRIKE3 consortium: Draft standards for receiver testing against threats. http://www.aic-aachen.org/strike3/downloads/STRIKE3_D42_Test_Standards_v2.0.pdf
- Peng, S., & Morton, Y. (2013). A USRP2-based reconfigurable multi-constellation multi-frequency GNSS software receiver front end. *GPS Solutions*, 17(1), 89–102. <https://doi.org/10.1007/s10291-012-0263-y>
- Qin, W., Dovis, F., Troglia Gamba, M., & Falletti, E. (2019, January). A comparison of optimized mitigation techniques for swept-frequency jammers. *Proceedings of the International Technical Meeting of The Institute of Navigation*, Reston, VA, 233–247. <https://doi.org/10.33012/2019.16691>
- Qin, W., Troglia Gamba, M., Falletti, E., & Dovis, F. (2019, September). Effects of optimized mitigation techniques for swept-frequency jammers on tracking loops. *Proceedings of the 32nd International Technical Meeting of the Satellite Division of The Institute of Navigation (ION GNSS+ 2019)*, Miami, FL, 3275–3284. <https://doi.org/10.33012/2019.17067>
- Raasakka, J., & Orejas, M. (2014, May). Analysis of notch filtering methods for narrowband interference mitigation. *Proceedings of the IEEE/ION Position, Location and Navigation Symposium (PLANS)*, Monterey, CA, 1282–1292. <https://doi.org/10.1109/PLANS.2014.6851503>
- Raimondi, M., Macabiau, C., & Julien, O. (2008, January). Frequency domain adaptive filtering against pulsed interference: Performance analysis over Europe. *Proceedings of the National Technical Meeting of The Institute of Navigation*, San Diego, CA, 164–176.
- Rao, M., O'Driscoll, C., Borio, D., & Fortuny, J. (2014). LightSquared effects on estimated C/N0, pseudoranges and positions. *GPS Solutions*, 18, 1–13. <https://doi.org/10.1007/s10291-012-0304-6>
- Rugamer, A., Joshi, S., van der Merwe, J. R., Garzia, F., Felber, W., Wendel, J., & Schubert, F. M. (2017, September). Chirp mitigation for wideband GNSS signals with filter bank pulse blanking. *Proceedings of the 30th International Technical Meeting of the Satellite Division of The Institute of Navigation (ION GNSS+ 2017)*, Portland, OR, 3924–3940. <https://doi.org/10.33012/2017.15289>
- Strang, G., & Borre, K. (1997). *Linear algebra, geodesy, and GPS*. Wellesley-Cambridge Press.
- Troglia Gamba, M., Falletti, E., Rovelli, D., & Tuozi, A. (2012, September). FPGA implementation issues of a two-pole adaptive notch filter for GPS/Galileo receivers. *Proceedings of the 25th International Technical Meeting of the Satellite Division of The Institute of Navigation (ION GNSS 2012)*, Nashville, TN, 3549–3557.
- Tsui, J. B. Y. (2004). *Fundamentals of global positioning system receivers: A software approach* (2nd ed.). Wiley-Interscience.
- Van Dierendonck, A. J. (1996). GPS receivers. In B. W. Parkinson, P. Enge, P. Axelrad, & J. J. Spilker, Jr (Eds.), *Global positioning system: Theory and applications. Vol. 1 of progress in astronautics and aeronautics* (pp. 329–407). American Institute of Aeronautics and Astronautics.
- Wang, S., An, J., Wang, A., & Bu, X. (2010). A minimum value based threshold setting strategy for frequency domain interference excision. *IEEE Signal Processing Letters*, 17(5), 501–504. <https://doi.org/10.1109/LSP.2009.2035414>
- Wendel, J., Schubert, F. M., Rügamer, A., & Taschke, S. (2016, September). Limits of narrowband interference mitigation using adaptive notch filters. *Proceedings of the 29th International Technical Meeting of the Satellite Division of The Institute of Navigation (ION GNSS+ 2016)*, Portland, OR, 286–294. <https://doi.org/10.33012/2016.14799>
- Willems, T., & De Wilde, W. (2013, January). Theory and practice of the interference mitigation technology (AIM+) in Septentrio receivers. *Proceedings of the International Technical Meeting of The Institute of Navigation*, San Diego, CA, 835–842. <https://www.ion.org/publications/abstract.cfm?articleID=10872>
- Young, J. A., & Lehnert, J. S. (1998). Analysis of DFT-based frequency excision algorithms for direct-sequence spread-spectrum communications. *IEEE Transactions on Communications*, 46(8), 1076–1087. <https://doi.org/10.1109/26.705409>
- Young, J. A., & Lehnert, J. S. (1999). Performance metrics for windows used in real-time DFT-based multiple-tone frequency excision. *IEEE Transactions on Signal Processing*, 47(3), 800–812. <https://doi.org/10.1109/78.747785>

How to cite this article: Borio D, Gioia C. GNSS interference mitigation: A measurement and position domain assessment. *NAVIGATION*. 2021;68:93–114. <https://doi.org/10.1002/navi.391>